

The Effects of Electrode Geometry on the Performance of a Micro-Pulsed Plasma Thruster Designed for a CubeSat

a project presented to
The Faculty of the Department of Aerospace Engineering
San Jose State University

in partial fulfillment of the requirement for the degree
Master of Science in Aerospace Engineering

by

Kwabena A. Boateng

Fall 2021

approved by

Dr. Periklis Papadopoulos
Faculty Advisor



© 2021
Kwabena Boateng
ALL RIGHTS RESERVED

ABSTRACT

The Effects of Electrode Geometry on the Performance of a Micro-Pulsed Plasma Thruster Designed for a CubeSat

Kwabena A. Boateng

For CubeSats there exists few propulsive options for station-keeping that keep the craft within the required weight and dimensions for the standardized CubeSat. Micro-Pulsed Plasma Thrusters (μ PPTs) provide a unique opportunity to apply precise thrust-bits that make this possible. The efficiency of μ PPTs, much like standard sized PPTs, is heavily dependent on the dimensional qualities of its components, most importantly the electrodes, that deliver the electric pulse to the propellant, in this case Teflon, to produce an electrodynamically accelerated plasma. Varying the ratio of the electrode gap h to the electrode width w effectively changes aspect ratio AR , or ratio of h to w . In this report, a μ PPT with a discharge energy of 3 J, capacitance of 2.7 μ F and discharge time of 4 μ s was designed and its aspect ratio increased from 1 to 4 by increasing h to investigate the effects of AR changes to the overall performance. The final investigation showed that increasing h , and subsequently AR , led to an efficiency at $AR = 4$ that was 10x greater than efficiency at $AR = 1$. This trend of performance increases was seen for all other performance values. Ultimately, at the optimized aspect ratio of 4, the impulse bit, specific impulse and propulsive efficiency came out to be 15.8 μ N-s, 420 s and 1.1 %, respectively.

TABLE OF CONTENTS

1	Introduction	11
1.1	CubeSats	11
1.2	Standard Pulsed Plasma Thrusters	11
1.3	Literature Review.....	12
1.4	Project Proposal	16
1.5	Methodology	16
1.6	Variable Project Architecture	16
2	Modified Electro-Mechanical Teflon Ablation Numerical Model	19
2.1	Micro-Pulsed Plasma Thruster Performance Parameters	19
2.2	Modified Electro-Mechanical Teflon Ablation Model Overview	21
2.3	Modified Ablation Model	22
2.3.1	First Ablation Stage.....	22
2.3.2	Second Ablation Stage.....	24
2.3.3	Third Ablation Stage	26
2.4	Modified Electro-Mechanical Model.....	27
3	Pulsed Plasma Thruster Performance Analysis.....	31
3.1	Pulsed Plasma Thruster Selection and Background.....	31
3.2	Overall μ PPT Performance Parametric Analysis.....	36
3.3	Capacitor Characteristics and Parametric Analysis	42
3.3.1	Capacitor Bank Design Considerations and Characteristics	42
3.3.2	Capacitor Parametric Analysis	45
3.4	Power Processing Unit Characteristics and Design Considerations	48
3.4.1	Overall Circuit Characteristics and Theory	48
3.4.2	DC-DC Conversion System	49
3.4.3	Ignition Spark Circuit	50
3.5	Electrode & Propellant Characteristics and Parametric Analysis.....	51
3.5.1	Electrode Characteristics and Necessary Background	51
3.5.2	Electrode Parametric Analysis.....	52
4	Full System Design Parameters.....	57
4.1	Overall System Performance Constraints	57
4.2	Capacitor Design Constraints and Parameter Selection.....	58
4.3	Power Processing Unit Design Constraints and Parameter Selection	59
4.4	Full System Parameters.....	62

4.5	Mass Bit and Gas-dynamic Impulse Approximation.....	62
5	Thruster Performance Analysis and Results	64
5.1	MATLAB Implementation	64
5.2	System Performance	64
5.2.1	Current and Voltage Transients.....	65
5.2.2	Performance Characteristics	68
6	Conclusion.....	73
6.1	Future Considerations	73
	References.....	74
	Appendix A – MATLAB Code.....	77

LIST OF FIGURES

Figure 1.1 - Generic schematic of a pulsed plasma thruster's components. [5]	12
Figure 1.2 - Labelled side-fed PPT configuration [7].....	13
Figure 1.3 - PPU circuit diagram and cross-section of Coaxial PPT	15
Figure 1.4 - 16.2 joule asymmetrical PPT test article side-view [17].....	18
Figure 2.1 - First ablation stage physical model schematic	23
Figure 2.2 - Second ablation stage physical model schematic.....	24
Figure 2.3 - Third ablation stage physical model schematic	26
Figure 2.4 - μ PPT model and LCR circuit schematic [10]	28
Figure 3.1 - TMIT-PPT and heritage PPT performance [15]	32
Figure 3.2 - Assembled breech-fed PPTCUP [24].....	32
Figure 3.3 - Side-fed PPTCUP.....	33
Figure 3.4 - Sketch of the side-fed PPTCUP electrode and propellant configuration.....	33
Figure 3.5 - Busek BmP-220 micro-pulsed plasma thruster [27]	34
Figure 3.6 - Mechanical design of the Dawgstar μ PPT flight unit [29]	34
Figure 3.7 - Flight configuration of the LES-6 PPT [31]	35
Figure 3.8 - Clyde Space CubeSat PPT test article [13]	35
Figure 3.9 - AV3 dPPT design configuration [33]	36
Figure 3.10 - <i>Isp</i> and <i>E'</i> performance comparison of worldwide PPTs [30].....	38
Figure 3.11 - Clyde Space CubeSat PPT comparison of impulse bit vs. discharge energy [24]..	39
Figure 3.12 - μ PPT trade comparison of impulse bit vs. discharge energy	39
Figure 3.13 - μ PPT Trade comparison of mass bit vs. discharge energy	40
Figure 3.14 - μ PPT trade comparison of impulse bit, specific impulse, and discharge energy....	40
Figure 3.15 - Specific impulse trend as a function of impulse bit	41
Figure 3.16 - PPT circuit diagram w/ current loops.....	44
Figure 3.17 - Capacitor and resistance voltage and current transient curves for a charging capacitor	44
Figure 3.18 - Capacitance & discharge voltage v. discharge energy of chosen μ PPTs.....	46
Figure 3.19 - Capacitance for three discharge voltages at various discharge energies.....	47
Figure 3.20 - PPT PPU full representative circuit diagram	48
Figure 3.21 - Diagram representation of transformer operation [34]	50
Figure 3.22 - PPT ignition spark diagram representation	51
Figure 3.23 - Inductance gradient as a function of electrode separation or width.....	53
Figure 3.24 - Inductance gradient for a range of electrode gaps at four electrode widths.....	54
Figure 3.25 - Specific impulse and energy density correlation plot for five discharge energies..	56
Figure 3.26 - Specific impulse and energy density correlation plot for specified impulse range.	56
Figure 4.1 - Current plot of Coletti μ PPT [13]	59
Figure 4.2 - Current plot of Pottinger μ PPT [36].....	59
Figure 5.1 - Current transient response when AR = 1	65
Figure 5.2 - Current transient response when AR = 4	66
Figure 5.3 - Current transient when AR = 1 of the designed μ PPT and Pottinger's μ PPT	66
Figure 5.4 - Current transient when AR = 3 of the designed μ PPT and Pottinger's μ PPT	67
Figure 5.5 - Voltage transient when the AR = 1 of the designed μ PPT and Pottinger's μ PPT	67
Figure 5.6 - Voltage transient when AR = 3 of the designed μ PPT and Pottinger's μ PPT.....	68

Figure 5.7 - Damping Ratio as a function of the aspect ratio for the designed μ PPT and Pottinger's μ PPT	69
Figure 5.8 - Impulse bit as a function of the aspect ratio for the designed μ PPT and Pottinger's μ PPT	69
Figure 5.9 - Specific impulse as a function of the aspect ratio for the designed μ PPT and Pottinger's μ PPT	70
Figure 5.10 - Propulsive efficiency as a function of the aspect ratio for the designed μ PPT and Pottinger's μ PPT.....	70
Figure 5.11 - Impulse bit as a function of an increasing aspect ratio by decreasing electrode width	71
Figure 5.12 - Specific impulse as a function of an increasing aspect ratio by decreasing electrode width	71
Figure 5.13 - Propulsive efficiency as a function of an increasing aspect ratio by decreasing electrode width.....	72

LIST OF TABLES

Table 3.1 - Performance qualities of eligible PPT and μ PPT	37
Table 3.2 - Capacitor type properties	43
Table 3.3 - Capacitor performance parameters	46
Table 3.4 - Electrode design and performance qualities of eligible PPT and μ PPT	55
Table 4.1 - Pre-constraint design parameters	58
Table 4.2 - Real-world properties of relevant capacitors [38]	58
Table 4.3 - Relevant PPU component properties	60
Table 4.4 - Full μ PPT system design parameters	62
Table 5.1 - Pottinger μ PPT design parameters [36]	65

SYMBOLS

Symbol	Definition	Units (SI)
μPPT	Micro-Pulsed Plasma Thruster	--
I_{bit}	Impulse Bit	$\mu\text{N/s}$
PTFE	Polytetrafluoroethylene	--
h	Electrode gap	mm
w	Electrode width	mm
l	Electrode length	mm
d	Electrode thickness	mm
T	Thrust	N
P	Power	W
I_{sp}	Specific Impulse	s
AR	Aspect Ratio	--
V_0	Initial Discharge Voltage	V
C	Capacitance	μF
η	Propulsive efficiency	%
T_{sp}	Specific thrust	$\mu\text{Ns/J}$
L_{pe}	Plate electrode geometry inductance	nH
μ_0	Magnetic vacuum permeability	N/A^2
F_L	Electro-dynamic thrust	N
F_A	Gas-dynamic thrust	N
m_{bit}	Ablated mass bit	μg
f	Pulse Frequency	Hz
\dot{m}	Mass flow rate	$\mu\text{g/s}$
v	Ablated mass velocity	m/s
g	Gravitational constant	m/s^2
W	Kinetic energy	J
E'	Discharge energy	J
T_p	Phase-transition temperature	K
T_{surf}	Ablation surface temperature	K
$S(t)$	Heat flux	W/cm^2
γ	Discharge ablation ratio	--
$V(t)$	Time-dependent discharge voltage	V
$I(t)$	Time-dependent discharge current	A
$T_s(x, t)$	Non-Fourier heat conduction	K
C_n	Heat capacity at n -th state	J/K
τ_{0n}	Thermal relaxation time at n -th state	S
ρ_n	Density at n -th state	kg/m^3
k_n	Thermal conductivity at n -th state	$\text{W/(cm} \cdot \text{K)}$
σ	Boltzmann constant	$\text{kgm}^2/\text{s}^2\text{K}$
V_a	Acoustic velocity	m/s
$T_s(L, t)$	Teflon surface temperature	K

L_1	First ablation stage length	cm
v_n	Velocity at the n -th state	m/s
$Q_n(x, t)$	Heat density at n -th state	W/cm^3
E_a	Activation energy	J
R	Universal gas constant	$J/(K \cdot mol)$
E_p	Specific depolymerization energy	J
ρ_0	Teflon mean density	kg/m^3
$m(t)$	Cumulative ablation mass	μg
R_T	Total circuit resistance	Ω
R_n	Resistance of n -th component	Ω
L_T	Total circuit inductance	nH
L_n	Inductance of n -th component	nH
t'	Discharge time	S
T_e	Electron temperature	K
n_e	Electron number density	m^{-3}
$\dot{x}(t)$	Current sheet velocity	m/s
$\ddot{x}(t)$	Current sheet acceleration	m/s^2
$m(t_0)$	Total accumulated ablation mass	μg
$\dot{m}(t)$	Cumulative ablation mass flow rate	$\mu g/s$
L'_{pe}	Plate electrode inductance gradient per pulse	$\mu H/cm$
α	Arbitrary constant	--
β	Arbitrary constant	--
C_T	Total circuit capacitance	μF
τ	General time constant	--
τ_n	Time constant at n -th stage	--
SW_n	Switch of n -th number	--
ζ	Damping ratio	--
ζ_{cr}	Critical damping ratio	--
L'	Full system inductance gradient	$\mu H/cm$
A_p	Propellant surface area	cm^2
I_{tot}	Total impulse	Ns
m_p	Total propellant mass	g
ϵ_e	Electrical resistivity of a copper electrode	kgm^3/s^3A^2
l_f	Full electrode length	Cm
ζ_{req}	Required system damping ratio	--
M_{sys}	Full system mass	g

1 Introduction

1.1 CubeSats

In recent years, interest in Cube-Satellites, or CubeSats, has vastly increased as a growing number of organizations, independent groups, states, and academic institutions see it as a cost-effective method to perform space research. Until recently, satellite development has been dominated by the United States, Russia, members of the EU, China, Canada, Japan, and India due to the economic requirements of this industry [1]. CubeSats present an alternative option for satellite developers who do not have the economic leverage to undertake development in the ways the previously stated entities can. Due to launch and development costs, in the past, CubeSats could still hold a six-figure price as high as \$250,000. In the present day, it is possible for a commercial enterprise or an academic institution to develop a CubeSat with a cost ranging from \$5000 to \$50,000 [2]. This significant decrease in cost has lowered the barrier for entry for many entities and has expanded the capability for space research in the public domain.

As more space research opportunities become available to more commercial and academic entities, there is likely to be an increase in the need for CubeSats to become a more versatile research platform. As they are today, many CubeSats do not include the same flight systems that can be found on larger Satellites. This is due to the sizing standard pioneered by California Polytechnic University (Cal Poly) and Stanford University students that states that a 1U (unit) CubeSat have dimensions $10 \times 10 \times 10 \text{ cm}^2$ and a mass of around 1 kg . This sizing standard exists to conform CubeSat designs to restrictions that make them compatible with the P-POD CubeSat launcher, also designed by this same team [3]. 1U and 3U remain as the most common form factors for CubeSats but 6U, 12U and 24U platforms have also been considered, though they are highly uncommon [4]. These size requirements restrict CubeSat's operational capabilities since they limit the qualities of onboard systems, like power, propulsion, and attitude controls.

1.2 Standard Pulsed Plasma Thrusters

In the case of propulsion, most developers choose to opt out of its inclusion in their CubeSat platforms since many propulsion systems are complex and can inhibit other flight operations that would then need to compensate for a heavier or larger propulsion system. As such there is a continual need for a simple, flight-tested, light-weight propulsion system that can fulfill flight qualifications, be it attitude or orbit adjustments, efficiently. As it stands today, there are many options available for CubeSat Propulsion, from the traditional cold gas, liquid rocket, and solid rocket thruster systems to the more unconventional small-form-factor-adapted systems like, resistojets, pulsed plasma thrusters, RF Ion thrusters, hall thrusters, and solar sails [4]. This report will focus on the design and performance characteristics of different configurations of a Pulsed Plasma Thruster (PPT).

Within the field of small satellite development, PPTs are a relatively old design concept, with research documented as early as the 1960s. Despite almost 60 years of research and development the PPT propulsion platform has seen fairly little improvement in its performance. As such, research that leverages an understanding of the mechanisms that govern pulsed plasma thruster

operation to design a more optimized system is valuable to the development of light-weight thrusters. The aim of this project and subsequent report is to do just that.

1.3 Literature Review

To best devise a methodology for design and performance enhancements, the PPT must first be deconstructed so that its function can be understood. While simple in concept, the physics that govern why PPTs work is increasing complex as you dive into each of its components. This presents a challenge for optimization and is likely the reason why this propulsion platform has seen so few efficiency upgrades in the past 60 years. Generally, a pulsed plasma thruster is a propulsion system that uses an arc discharge, generated by a pulse of electricity from a capacitor, across a propellant surface between two electrodes (anode and cathode) to produce thrust. This arc discharge ablates and ionizes the propellant surface bit and produces a plasma that accelerates from the surface out of the exhaust of the PPT, producing thrust. The plasmas acceleration is mainly driven by a Lorentz Force created by the arc discharge and induced electro-magnetic field. The pulse of current generated by the capacitor usually lasts a few micro-seconds and is usually discharged approximately once per second [4]. Fig. 1.1 shows the schematic of a simple PPT which contains a spring mechanism, solid propellant (in this case Teflon), igniter plug, cathode, anode and capacitor [5]. The chemical name for Teflon is polytetrafluoroethylene, which will later be referred to as PTFE, but also as just Teflon. The efficiency of this PPT and others like it, is typically measured in impulse-bit I_{bit} or I_b , which is the average measured impulse for each “bit” of arc pulse that the PPT undergoes [6].

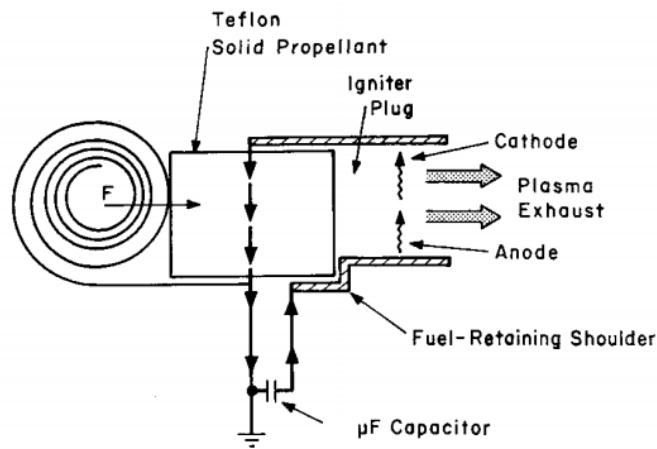


Figure 1.1 - Generic schematic of a pulsed plasma thruster's components. [5]

In 1970, an analysis on the performance characteristics of the PPT platform shown in Fig. 1.1, above, was performed by Robert J. Vondra, Keith Thomassen, and Albert Solbes of MIT based on the type of PPT that was previously deployed on the Lincoln Laboratory Satellite, LES-6 a year earlier. This analysis of a flight heritage PPT serves as an initial benchmark for future analyses and the conclusions from their report reveal later confirmed trends in PPT performance. The report concluded that there exists a linear relationship between the capacitors stored energy and the

specific impulse observed by the thruster. In one of the ablation tests, it was found that a 5000 A current pulse, with an impulse bit $I_{bit} = 32 \mu Ns$, ablates 0.00000001 kg of the PTFE. Only 3/40ths of the ablated PTFE actually ionizes and accelerates, while the remaining ablated PTFE exists as neutrals “oozing” off of the propellant surface. Almost 70% of the energy used in this process is expended on heat loss in the electrode, propellant ablation and molecule dissociation, and ionizing plasma heating electrons (which takes up most of that 70%). This results in a propulsion system where only 2.96% of the energy put into the system is converted to thrust, with approximately 32% of the input energy dissipated in the capacitor. This experimental result is one of the first in a long trend of results over the next 50 years that confirm the low efficiency of the PPT compared to other forms of small satellite propulsion. [5]

The thruster used in the MIT study would become known as a breech-fed PPT, meaning the propellant is fed through an opening between the electrodes via a spring load to the rear of the propellant. The resulting plasma plumes propagate along the electrode and out of the opening. This propellant fed system is only one of many different kinds of propellant feed systems that would later be developed. Other, later developed, configurations of PPT include side-fed, coaxial and breech-fed with a V-shaped ablation. V-shaped ablation breech-fed and side-fed PPTs were the next configurations to appear. As early as the mid-1970s, the research on PPTs began looking into how changes in geometry effect efficiency. Making variations to the electrode spacing h , the propellant gap/width w and the electrode angle ϕ researchers could boost thrust efficiency up to 53% with a 1280 s specific impulse. Specifically, the efficiency increases when ϕ sees a, no greater than, 20% increase and h/w increases. These factors can be seen in Fig. 1.2 on a side-fed PPT. The Mykroy shield in the figure is an insulative material that functions as a way to focus the propellant ablation. [7]

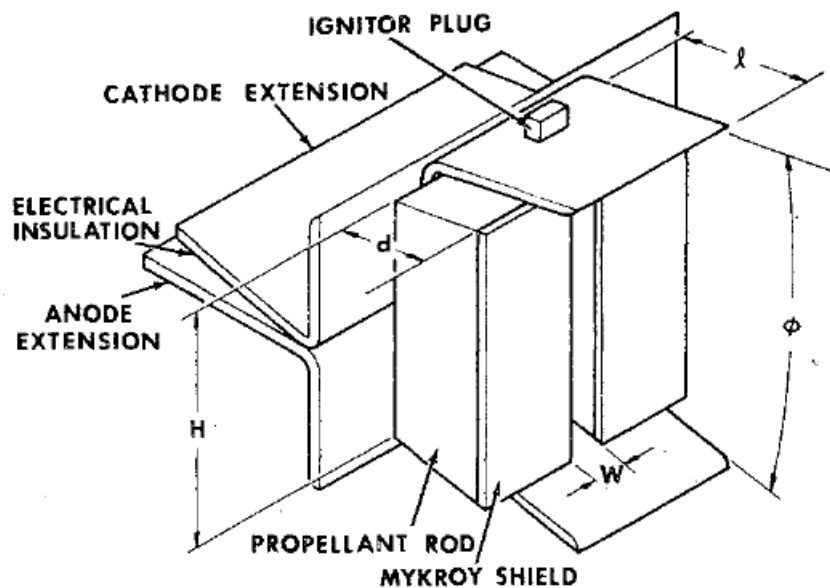


Figure 1.2 - Labelled side-fed PPT configuration [7]

One of the critical design criteria for the PPT appears to be the aspect ratio, which is the ratio between the thrust T and power input P . This value is also proportional to the earlier mentioned electrode geometry ratio h/w , as seen in Eq. 1.1 below. [8]

$$\frac{T}{P} \propto \frac{h}{w} \quad (1.1)$$

This efficiency is not without limit. It is known that a high aspect ratio will lead to propellant charring which significantly decreases the efficiency of the PPT. Considering breech-fed PPTs with flight heritage, it is possible to set an effective area ratio between 0.7 and 7 [8]. Furthermore, it has been shown that thruster performance is also dependent on which parameter (h or w) is changed in order to increase the aspect ratio. Based on a detailed experimental analysis on electrode and propellant geometry by Yuan-Zhu Kuan, it can be shown that, below a certain aspect ratio, the impulse bit will decrease with increasing aspect ratio by changing w . This report also shows that above a certain aspect ratio, changing h to increase the aspect ratio will also increase the impulse bit [9]. This information is valuable since the objective of this project is to miniaturize the standard PPT model to fit within a CubeSat qualified form factor which means decreasing the area of the exposed propellant and adapting the aspect ratio to accommodate for this change.

PPT that are miniaturized to fit within a CubeSat qualified form factor are classified as micro pulsed plasma thrusters (μ PPT). While a linear relationship can be seen between propellant size and impulse-bit, miniaturization could drastically impact the thrust and overall efficiencies of a PPT. Fortunately, extensive research is available that verifies flight heritage μ PPT performance and presents analysis structures for μ PPT modeling and simulation. Among standard PPT models there exists a very common, mature model: the electromechanical model. This model approximates that the PPT is an electromechanical device with an electric circuit that interacts with a dynamic system. That said, most iterations of this model fail to accurately factor the ablation process for a PPT. To counter this, researchers Yang Ou, Jianjun Wu, Yu Zhang, Jian Li and Sheng Tan developed a numerical method that merges the PTFE ablation model with a modified electromechanical model. This model theoretically idealizes the electric circuit as a Lenz-Capacitor-Resistance (LCR) circuit with discrete elements and an ablation process with heat conductivity, phase transition, non-Fourier effect and material reflectivity factored in [10]. This entire process works to numerically model a scaled down PPT without introducing inefficiencies due to the scaling process itself. The design standards set by this modeling process make it possible to set a desired approximate performance characteristic and then build a μ PPT using components that satisfy these characteristics.

Picking μ PPT components to satisfy previously decided design requirements entails having an expansive understanding of the performance characteristics of various configurations of each of its components. With the propellant this means analyzing the performance of coaxial vs rectangular geometries. The rectangular propellant geometry, seen in Fig. 1.1, is the most common and well researched form of propellant geometry while coaxial configurations have seen a growth in popularity in the past 10 years within the testing environment. Coaxial propellant PPT follow the same functional principals as rectangular propellant PPTs. The difference between them is that with the coaxial PPT the central electrode (anode) is cylindrical, while the outer electrode (cathode) is ring shaped with the solid propellant filling the space in between the electrodes [11]. Not only that, but in recent years the chemical composition of test PPT propellant has been shifting from the extremely common PTFE to other forms of solid propellant often called high-performance electric propellant (HIPEP). [11]

Along with having different chemical compositions, rectangular and coaxial propellant geometries also hold different performance qualities. Historically, with the use of PTFE, rectangular geometry PPTs have shown to have higher efficiencies, around 15%, compared to PPTs with a coaxial geometry, around 7% [12]. In recent years, both rectangular and coaxial PPT geometries have seen an increase in performance capability as other forms of ignition, geometries, and propellant types are researched and tested. In some cases, an efficiency of 50% has been achieved during thrust tests, as is with a recently tested Pulsed inductive thruster which boasts an I_{sp} as high as 8000 s [12].

Another PPT component that must be considered before miniaturization is the electrodes. In the testing environment, it has been shown that material composition and geometry have a considerable effect on the performance of standard PPTs. This is also true for μ PPTs. The most common material used for PPT electrodes is copper alloy, usually Tungsten-plated. This is due to its low electrical resistivity, lower rates of erosion and advantageous mechanical and thermal properties [13]. That said research in the past 20 years has investigated the viability of other materials like aluminum alloy, brass, and molybdenum [14] [15]. After material is considered an electrode geometry must also be chosen. The two dominant electrode geometry configurations are the coaxial and parallel plate configurations. Both of these types can further be configured to enhance performance. For example, the parallel plate is the most common electrode geometry used with breech-fed PPTs. Other variations of this geometry include angled plates, like in Fig. 1.2 and, the more recently studied, asymmetrical plate [16]. Coaxial electrodes, shown below in Fig. 1.3, tend to remain in simple in design, but recent research suggests that making modifications to the tip geometry to the inner cylindrical electrode (anode) can benefit PPT performance [15]. Each of these geometries work to hinder or help the propulsion efficiency of the PPT and for this report they will be simulated and tested to assess each configuration's performance qualities.

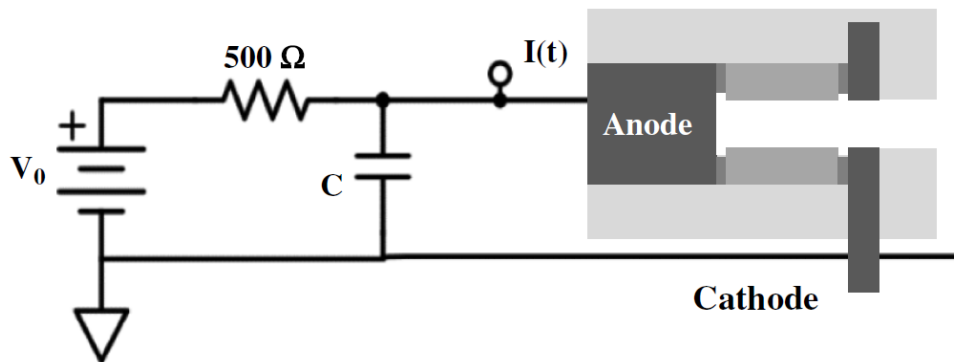


Figure 1.3 - PPU circuit diagram and cross-section of Coaxial PPT

Other than the electrode and propellant geometry and material, the capacitor which functions adjacent to the power processing unit (PPU) remain as the primary way energy is input into the system. Most diagrams of the circuit layout of the PPU will show the capacitor as the sole component of that system, when, in reality, the system needed is more complex. In standard lab bench-top PPT, it is common to maintain a relatively simple design like the one in Fig. 1.3, which was made for a coaxial PPT test article. This configuration features a power source V_0 that charges the capacitance C through a 500Ω charging resistor. The capacitance C is made up of a bank of

eight $1\mu\text{F}$ capacitors that are rated up to 2.4 kV [11]. Flight heritage PPTs and μPPT s have PPUs with a similar structure with a more complex array of components.

1.4 Project Proposal

With the research benchmarks in mind, the objective of this report is to investigate the trends in efficiency, specific impulse, and impulse-bit of a low power micro-pulsed plasma thruster with progressively adapted non-conventional electrode and propellant geometries applied to its design. This is all done in order to design a complete μPPT with fixed component properties except for electrode and propellant geometries which will be varied within an analysis of its effects on overall performance.

1.5 Methodology

Before the design process for the PPT test articles needed for this investigation can begin, a numerical model for predetermining the performance must be chosen. Using this numerical model, computation of the desired performance values can be performed from which design specifications can be ascertained. In order to produce a standard test platform from which multiple propellant and electrode geometries can be tested, the PPU of each test configuration must be identical. This means that the input values for each configuration must be the identical. Then a trade study will be done with previously tested μPPT to identify an ideal sizing constraint for the whole system and each component in it. Another trade study will be performed with previously tested μPPT to identify ideal materials and geometries for the electrode and propellant block. From these trade studies, the final configuration of each component of the system will be chosen. Then comes their design. Each test configuration will be designed with CAD software based on the chosen design configuration. Based on previous test architectures a test stand will be designed to capture the performance qualities of the test article. After this design process, parts will be acquired, built to design standards, and calibrated for operation. Finally, a test will be run on the test stand, performance data will be consolidated, and plots of the impulse bit, specific impulse, propulsive efficiency, and overall efficiency will be produced after extrapolating data and computing the results. While the scope of this may narrow or expand depending on the available resources, the previously stated process will remain as the foundational method for this project's execution.

1.6 Variable Project Architecture

There are three possible levels of complexity for the research, experimentation and reporting that can be conducted for this project. Each level meets the qualifications necessary for an acceptable project that fulfills the objective laid out in the project proposal but increases in its level of complexity and/or necessary components. These levels will fulfill the objective for this project as follows:

- Level 1 – Primary Objective
- Level 2 – Intermediate Objective
- Level 3 – Advanced Objective

The primary objective contains the tasks necessary for successfully completing an acceptable project report. The intermediate objective contains all the tasks of the primary objective plus more research, experimentation and reporting that expands on the primary objective's primary goals. Lastly, the advanced objective contains all the tasks of the intermediate objective plus more research, experimentation and reporting that expands on the intermediate and primary objective's primary goals. The fundamental factors that will decide which one of these objectives can be completed are time, logistics and availability of resources (like money, lab tools, and test space). The primary objective is the minimum requirement for this project and is, ideally, designed to guarantee results before the end of the project period.

The primary objective of this project is to study the effects of different combinations of electrode geometries on a breech-fed propellant-type μ PPT. It is already shown that an increase in the propellant aspect ratio will produce an increase in the impulse-bit for a standard PPT [7]. Since research for this in μ PPT is limited, it is valuable to know if the performance limits for the propellant aspect ratio in μ PPT are similar to those in standard PPT. This process would entail applying the numerical model for parameter analysis devised by Yang Ou and Jianjun Wu. This model was specifically designed for breech-fed μ PPT with parallel plate electrodes and functions as both an electromechanical and Teflon ablation model [10]. Its creators have not given it a name but for the sake of expediency in this report, this model will be referred to as the Modified Electro-Mechanical and Teflon Ablation model (MEMTA). Using the MEMTA model provides a basis for the design of each μ PPT test article and the parameters of its components.

For the sake of completing the primary objective for this project, five test articles need to be designed and analyzed. One will have an aspect ratio that is slightly lower than the intended limit for PPT – which is around 1.0 – and another will have an aspect ratio slightly higher than the intended limit for standard PPT – which is around 4.0 [8]. The last 3 will have varying propellant aspect ratios ranging between 1.0 and 4.0. Since the relationship between impulse and aspect ratio is relatively linear [5], the aspect ratios between these test articles will be evenly spaced. This variation of the aspect ratio is reflective of a variation in the propellant geometry as well as the electrode geometry. That said, the length of the pulse/discharge chamber, which extends from the propellant surface out along the electrodes, will remain the same across all test articles. The same will also be true for the design parameters of the PPU, the electrode angle φ , electrode thickness d and the materials chosen for each component. This will help to lower the probability of efficiency discrepancies due to varying test article design. This experiment is designed so that the limits of PPT performance can be compared with μ PPT performance in order to understand the difference between the two.

The intermediate objective will include every process involved in completing the primary objective while also using the primary objectives results as a comparison benchmark for a new experiment that seeks to improve the PPTs efficiency. This new experiment is based off of research that asserts that asymmetrical electrode geometries result in increased PPT performance [16] [17]. The “asymmetrical” modifier for this PPT type refers to the length of the electrodes past the propellant surface. In most PPT with a parallel electrode configuration, the length of the cathode and anode past the propellant surface is identical. This PPT type is designed in a such way that one

electrode is longer than the other, shown in Fig. 1.3. Preliminary research on this type of PPT (Fig. 1.3) claims that PPTs with a segmented anode experience an improvement in the impulse bit of up to 28% and a 49% improvement in thrust efficiency [17]. This research experiment was done on a standard PPT, so it would be advantageous to understand how this change will affect μ PPTs.

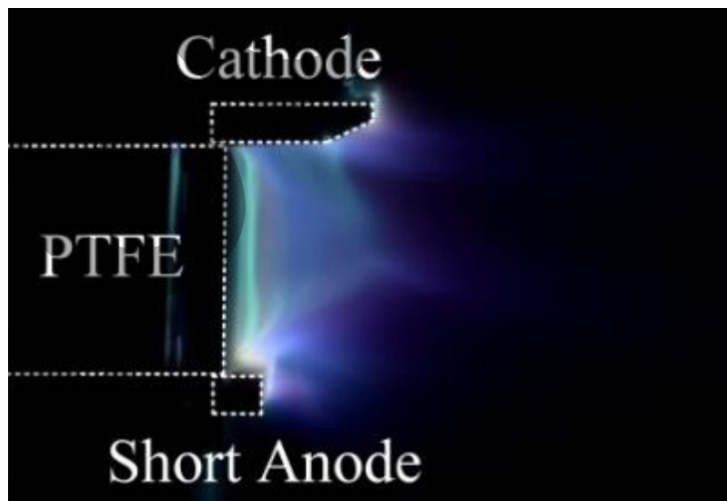


Figure 1.4 - 16.2 joule asymmetrical PPT test article side-view [17]

For the sake of the intermediate objective, the asymmetric electrode geometry will be tested with five different μ PPT test articles. Each one of these five test articles will retain the same design parameters (varied aspect ratio, PPU design, cathode length and width, propellant type and component material) as those chosen for the primary objective but the anode for these articles will be segmented to a pre-determined length. This will allow for the primary objectives results to function as a preliminary benchmark from which performance comparisons can be made. This allows for two modes of comparison: the performance of standard PPT test articles vs. this one and the performance of the primary objectives μ PPT test articles vs. with this one (intermediate objective).

Lastly, the advanced objective will include every process involved in the primary and intermediate objectives while increasing the variance of both experiments in order to increase the data points in each objectives result, thus increasing the accuracy of the results. This means adding five more test articles to each objectives experiment that have aspect ratios in between the values of the previously tested μ PPT. Furthermore, the advanced objectives next goal will be to take the asymmetrical electrode test article with the greatest efficiency improvement and adjust the anode segment length to discover its effects on performance. It is likely that there is a limit to how close the anode can be to the propellant surface. This objective seeks to investigate the likely hood of this assertion and compare its test results with the previously tested μ PPT geometries in this project. This means changing the anode length across 4 different test articles, based on a range of anode lengths used in previously tested asymmetric μ PPT. The advanced nature of this objective lies not in its complexity but rather the sheer number of repeated experiments that are needed to complete the objective. In fact, the greatest challenge of this objective is to ensure that all the test articles produced for this experiment are relatively identical as to not introduce major performance discrepancies across multiple articles.

2 Modified Electro-Mechanical Teflon Ablation Numerical Model

For the sake of designing a μ PPT that satisfies the operational requirements needed to qualify as valid test article, it is imperative that an understanding of the functional characteristics of a valid μ PPT is formed. One way of achieving this is to perform a trade study on the individual performance qualities of previous iterations of flight heritage μ PPT and validated μ PPT test articles. This is the method that is utilized for this project and is documented later in this report. Another method for understanding μ PPT performance and operation would be to derive a numerical model of its operation based on the physical properties that govern its working processes. This chapter is an overview of the numerical method that was utilized to assist in the design qualification and optimization of the μ PPT test articles needed for this project, as well as the underlying math that governs general PPT operation. This numerical method was devised by Yang Ou, Jianjun Wu and their associates at the National University of Defense Technology in Changsha, China. It consolidates a modified electro-mechanical model with a modified two-layer ablation model in order to produce a high precision μ PPT model while also considering the non-Fourier effects μ PPT ablation. Solving the derived equations in this method, it is possible to obtain the values of the major performance parameters for a considered μ PPT. [10]

2.1 Micro-Pulsed Plasma Thruster Performance Parameters

The performance parameters generally used to understand the performance qualities of μ PPT test articles and flight models are its specific impulse I_{sp} , impulse-bit I_{bit} , thrust-to-power ratio T/P – or specific thrust T_{sp} , and propulsive efficiency η . They are heavily dependent on the geometric and operational characteristics of the μ PPT, namely its electrode, propellant, and capacitor parameters. Likely the most important parameter of the μ PPT, and the focus of this report, the electrode geometry plays a pivotal role in modifying the performance of a PPT. Its length, width and gap have a great influence on efficiency. The inductance of parallel plate electrodes, which are the type used in breech-fed μ PPT can be generally defined in Eq. 2.1 where L_{pe} is the plate electrode geometry inductance, μ_0 is the magnetic vacuum permeability, h is the electrode gap, w is the electrode width and l is the electrode length. This equation will be further expanded utilizing the MEMTA method. [10][18]

$$L_{pe} = \mu_0 \frac{h}{w} l \quad (2.1)$$

The thrust that is produced by the arc discharge process along the electrodes can be split into two major force components: electromagnetic forces and gas dynamic forces as shown in Eq. 2.2. The thrust due to electromagnetic forces, which in this case is defined as the Lorenz force F_L , can be generally defined as it is in Eq. 2.3, where f is the pulse frequency and i is the total current in the LCR circuit model. This equation with also be further evaluated to represent the current as a function of time. [10][18]

$$T = F_L + F_A \quad (2.2)$$

$$F_L = f \frac{\mu_0 h}{2 w} \int_0^t i^2 dt \quad (2.3)$$

The thrust due to the gas dynamic expansion F_A , can generally define as it is in Eq. 2.4, where γ is the specific heat capacity ratio, which for Teflon is 1.3, m_{bit} is the mass of the ablated propellant and E is the capacitor discharge energy [18]. This derived form of the gas dynamic force is a preliminary expression and will be further derived in the MEMTA numerical method as a function of the electrode geometry.

$$F_A = f \left[\frac{8(\gamma - 1)}{\gamma^2(\gamma + 1)} m_{bit} E' \right]^{1/2} \quad (2.4)$$

The capacitor discharge energy E needed to find the gas dynamic thrust in Eq. 2.4 can be defined as function of the capacitance C and voltage needed for discharge or discharge voltage V_0 , as such:

$$E' = \frac{1}{2} C V_0^2 \quad (2.5)$$

The thrust can also be defined as a function of the pulse frequency f and the impulse bit I_{bit} , as seen below in Eq. 2.6:

$$T = I_{bit} f \quad (2.6)$$

After establishing the definition for the thrust of a PPT, it is now possible to define the performance parameters within their appropriate context. First, the specific impulse can be initially defined as a function of the total thrust T , ablated propellant mass flow rate \dot{m} and the gravitational constant, as seen in Eq. 2.7, but can be further derived to be a function of the I_{bit} , m_{bit} , and g . This can be seen in Eq. 2.8. The impulse bit can be defined as a function of the ablated propellant mass and the velocity of the ablated propellant mass, shown in Eq. 2.9. [18]

$$I_{sp} = \frac{T}{\dot{m}g} = \frac{T/f}{m_{bit}g} \quad (2.7)$$

$$I_{sp} = \frac{I_{bit}}{m_{bit}g} \quad (2.8)$$

$$I_{bit} = m_{bit}v \quad (2.9)$$

From here, the thrust efficiency can be defined. In general, the thrust efficiency is the ratio of the utilized energy in propulsion to the total input energy. In this case, it is the ratio of kinetic energy of the ablated propellant W to the capacitor discharge energy E' , shown in Eq. 2.10. Specifically, W is the kinetic energy equation (Eq. 2.11) but it can be further evaluated using Eq. 2.9 to be a function of the impulse bit and the total ablated mass per pulse. This formation of the equation is also shown below in Eq. 2.12.

$$\eta = \frac{W}{E'} \quad (2.10)$$

$$W = \frac{1}{2}m_{bit}v^2 \quad (2.11)$$

$$W = \frac{I_{bit}^2}{2m_{bit}} \quad (2.12)$$

When Eq. 2.10 and 2.12 are applied to each other we get a resultant thrust efficiency that looks like this:

$$\eta = \frac{I_{bit}^2}{2m_{bit}E'} \quad (2.13)$$

2.2 Modified Electro-Mechanical Teflon Ablation Model Overview

The previously mentioned performance parameters have been presented in their general format. Moving forward, the MEMTA numerical model will be presented and by the end, each performance parameter will be modified to the model's design constraints. Like previously mentioned, the modified electro-mechanical Teflon ablation (MEMTA) model was derived by Yang and Jianjun in order to present to a numerical method that overcomes some of the shortcomings of previous PPT numerical models. Its key characteristic is that it can calculate the ablation mass accumulation of the work fluid while taking non-Fourier effect heat conduction into account [10]. This is important to the analysis of μ PPT because Fourier's law, while still a powerful tool for the analysis of most heat conduction and mass diffusion problems, cannot be accurately applied to analyze heat conduction within extremely short periods of time [19]. Since arc pulses in PPT and μ PPT alike occur on time scales in the micro- and milli-second range it is imperative the applied numerical model be able to "handle" the significantly low heat flux involved.

The MEMTA method models non-Fourier analysis of heat conduction, while also considering material reflectivity, phase transition, material inductance and resistance, capacitance and electrode geometry. To do this, the MEMTA model requires splitting the analysis into two distinct parts: a modified ablation model and a modified electro-mechanical model. The ablation model portion of the MEMTA model is an analysis of three stages of ablation that considers the solid, gel and plasma phases of Teflon during arc discharge ablation. Out of this process, it is possible to

derive the cumulative ablation mass as a function of time. This value becomes the input parameter of the modified electro-mechanical model which acts to simulate the operation of the μ PPT (outside of ablation). It from this simulation that the essential μ PPT performance parameters can be derived. [10]

2.3 Modified Ablation Model

The modified ablation model that makes up the foremost portion of the MEMTA model is designed to demonstrate how the heat conduction and phase-transition processes contribute to the multi-layered ablation produced by arc discharge across the propellant surface. This process is initiated by a spark plug which induces the arc discharge and heats the surface the propellant (Teflon in this case). With a phase-transition temperature (T_p) of 600 K, the Teflon will eventually undergo a phase transformation that is, in this model, delegated to three different ablation stages. [10]

In the first ablation stage, the arc discharge has not yet heated the ablation surface T_{surf} to T_p so the phase transition process has also not yet occurred. Here a single-layer thermal model is applied to model the temperature distribution through heat conduction. Once, T_{surf} is raised to T_p , the phase-transition process occur in what can now be considered the second ablation stage. For this stage, a two-layer ablation model is utilized. The two layers involved are the solid and gel Teflon layers which also form a melting phase interface in between. This new gel layer exists as a result of a portion of the solid-crystalline Teflon going through a phase transition to this amorphous state. The rest of the phase-transitioned Teflon is repelled off the gel-phase Teflon's surface as ablated plasma. After this process ends and the arc discharge dissipates, the Teflon will begin cooling. At this point, the temperature can still be high enough to cause ablation in a process known as delayed ablation. This final, cooling, and delayed ablation process occurs during the third, and final, ablation stage. [10]

2.3.1 First Ablation Stage

In the first ablation stage, as previously mentioned, the Teflon is heated up, but phase transition does not occur since T_{surf} has not surpassed T_p . Fig. 2.1 shows that at the surface of the Teflon, where $x = L$, a heat flux $S(t)$ from the arc discharge is introduced that induces heat conduction in the solid-state Teflon.

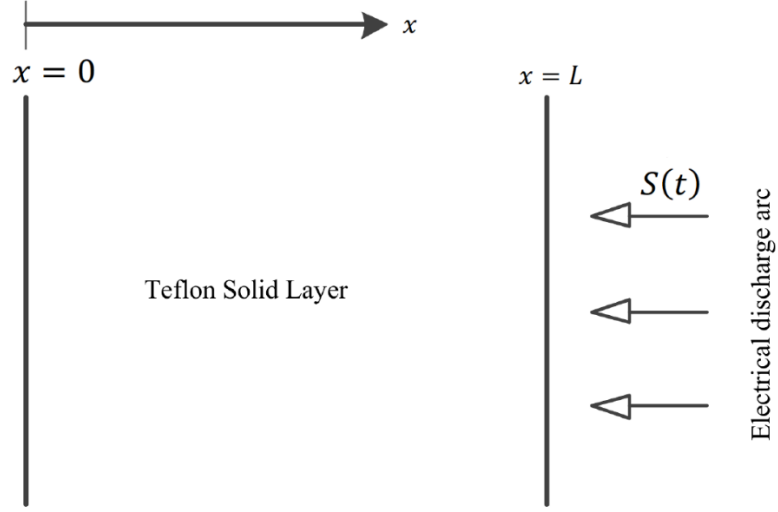


Figure 2.1 - First ablation stage physical model schematic

The heat flux acting on the Teflon surface can be expressed in the way that it is in Eq. 2.14, where γ is the ratio of the single pulse discharge energy absorbed by the surface of the Teflon solid, $V(t)$ is the capacitor discharge voltage function and $I(t)$ is the discharge current function. [10]

$$S(t) = \frac{\gamma V(t) I(t)}{hw} \quad (2.14)$$

The temperature distribution in the Teflon solid due to non-Fourier heat conduction $T_s(x, t)$ can be characterized in Eq. 2.15. In this equation, ρ_s is the solid-state density for Teflon, C_s is the solid-state heat capacity for Teflon, and k_s is the solid-state thermal conductivity for Teflon. The term τ_{0_s} is the thermal relaxation time of solid-state Teflon and can be found using Eq. 2.16, where V_a is the acoustic velocity. [10][21]

$$\frac{\partial[\rho_s C_s T_s(x, t)]}{\partial t} + \tau_{0_s} \frac{\partial^2[\rho_s C_s T_s(x, t)]}{\partial t^2} = \frac{\partial}{\partial x} \left(k_s \frac{\partial T_s(x, t)}{\partial x} \right) \quad (2.15)$$

$$\tau_{0_s} = \frac{3k_s}{\rho_s C_s V_a^2} \quad (2.16)$$

At the rear surface of the solid-state Teflon, where $x = 0$, there is a boundary condition that is defined in Eq. 2.17. At the front exposed surface of the solid-state Teflon, where $x = L$, there is a boundary condition that is defined in Eq. 2.18. In this condition, σ is the Boltzmann constant, ε is the absorption coefficient of the working mass ablation surface and $T_s(L, t)$ is the surface temperature of the Teflon solid (where $x = L$). [10][21]

$$-k_s \frac{\partial T_s(x, t)}{\partial x} \Big|_{x=0} = 0 \quad (2.17)$$

$$-k_s \frac{\partial T_s(x, t)}{\partial x} \Big|_{x=L} = S(t) - \sigma \varepsilon [T_s(L, t)]^4 \quad (2.18)$$

2.3.2 Second Ablation Stage

The ablation process reaches the second stage once T_{surf} has exceeded T_p . The ablation surface of the Teflon will then undergo a phase transformation that will leave the non-ablated Teflon material in with two compositions: the solid and gel layers (shown in Fig. 2.2). The solid layer while extending a shorter distance along x than in the first ablation stage, maintains the same thermal properties and required temperature distribution analysis from the first ablation stage. The gel layer, however, extending off the surface requires further calculation to expand the necessary temperature distribution analysis. In between the two layers is a melting phase interface at $x = L_m$ which will need to be defined as a boundary in the analysis. During this stage, as well, the length of the non-ablated Teflon from the first stage (L) is represented as L_1 . Additionally, the moving velocity of the exposed Teflon ablation surface is v and the moving velocity of the melting phase interface is v_m . [10][21]

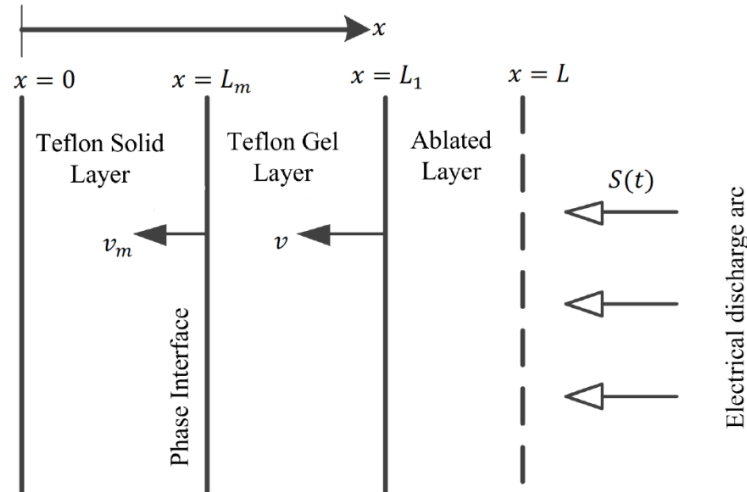


Figure 2.2 - Second ablation stage physical model schematic

Since the solid-state Teflon temperature distribution has already computed, all that is left for this ablation stage is to find the temperature distribution of the gel-state Teflon, $T_m(x, t)$. This process is shown in Eq. 2.19. The terms ρ_m , C_m , τ_{0m} , and k_m are the gel-state Teflon's density, heat capacity, thermal relaxation time and thermal conductivity, respectively [20]. Also, the term τ_{0m} , is defined in Eq. 2.20. The last term in the equation, $Q_m(x, t)$, is the energy released per unit time and volume (W/m^3) [21]. The equation for this term is given below in Eq. 2.21, where A_p is

the pre-exponential factor, E_a is the activation energy, R is the universal gas constant, and E_p is the specific depolymerization energy [10].

$$\frac{\partial[\rho_m C_m T_m(x, t)]}{\partial t} + \tau_{0_m} \frac{\partial^2[\rho_m C_m T_m(x, t)]}{\partial t^2} = \frac{\partial}{\partial x} \left(k_m \frac{\partial T_m(x, t)}{\partial x} \right) + Q_m(x, t) \quad (2.19)$$

$$\tau_{0_m} = \frac{3k_m}{\rho_m C_m V_a^2} \quad (2.20)$$

$$Q_m(x, t) = -A_p \rho_m E_p \exp\left(-\frac{E_a}{RT_m(x, t)}\right) \quad (2.21)$$

The boundary condition of the gel-state ablation surface can be seen is Eq. 2.22 below, where \dot{m} is the mass flux coming from the exposed Teflon ablation surface and L_1 from Fig. 2.2 above is the farthest bound of the Teflon article in the $+x$ -direction. [10]

$$-k_m \frac{\partial T_m(x, t)}{\partial x} \Big|_{x=L_1} = S(t) - \sigma \varepsilon [T_m(L_1, t)]^4 - \dot{m} C_m T_m(L_1, t) \quad (2.22)$$

The mass flux \dot{m} can be found by performing the integration in Eq. 2.23 across the entire gel, or amorphous, region, where the location of the melting phase interface L_m at a specific time, can be found using the formulation in Eq. 2.24, where v_m is the moving velocity of the melting phase interface. [21]

$$\dot{m} = A_p \int_{L_m}^{L_1} \rho_m \exp\left(-\frac{E_a}{RT_m(x, t)}\right) dx \quad (2.23)$$

$$L_m = L_1 + \int_{t_m}^t v_m dt \quad (2.24)$$

The moving velocity of the melting phase interface v_m can be seen below in Eq. 2.25, where H_0 is the total enthalpy of the solid-to-gel phase transition of Teflon and ρ_0 is the mean density of the whole Teflon article (both solid and gel layers). [10]

$$v_m = \frac{1}{\rho_0 H_0} \left[k_s \frac{\partial T_s(x, t)}{\partial x} \Big|_{L_m^-} - k_m \frac{\partial T_m(x, t)}{\partial x} \Big|_{L_m^+} - S(t) \right] \quad (2.25)$$

Lastly, the moving velocity of the Teflon ablation surface, also known as the recession velocity, v , is expressed in Eq. 2.26, where ρ_r . The distance the Teflon ablation surface travels during ablation (ΔL) is dependent on its velocity and can be seen in Eq. 2.27, where t' is the time of a single pulse. With this the value of L_1 can also be found using Eq. 2.28. [10]

$$v = -\frac{\dot{m}}{\rho_r} \quad (2.26)$$

$$\Delta L = \int_0^{t'} v dt \quad (2.27)$$

$$L_1 = L - \Delta L \quad (2.28)$$

2.3.3 Third Ablation Stage

In the final ablation stage, the arc discharge that has been inducing a heat flux on the Teflon ablation surface has ended and the Teflon subject is cooling. If the temperature of the Teflon solid is still high, it will continue to in a process called delayed ablation. In this case L_2 , becomes the farthest bound of the non-ablated Teflon article in the x -direction. A schematic of this stage can be seen below in Fig. 2.3.

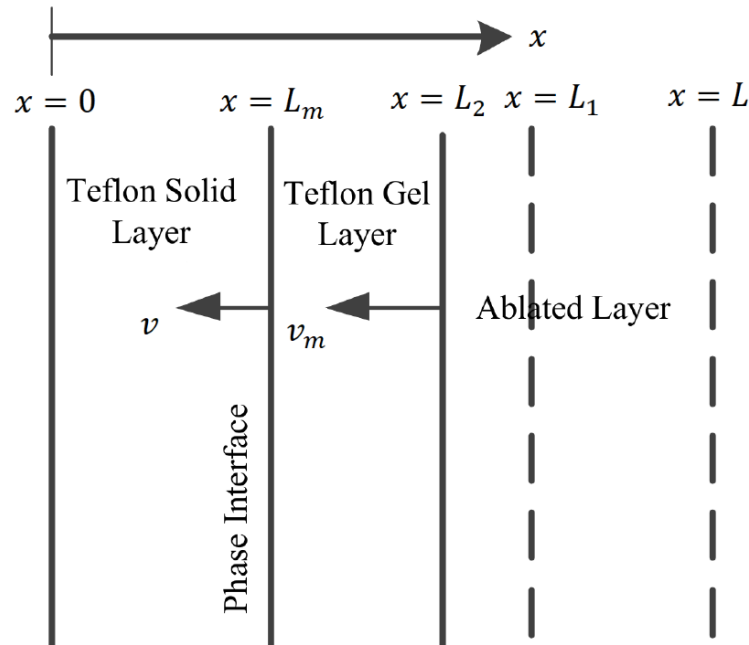


Figure 2.3 - Third ablation stage physical model schematic

When the temperature of the Teflon article is high enough for ablation, the temperature distribution can be expressed using Eq. 2.29 and the boundary condition at the Teflon ablation

surface is defined by Eq. 2.30. At a low temp, the temperature distribution resembles that of solid-state Teflon and the boundary conditions are the same. Both of these are expressed in Eq. 2.31 and 2.32, respectively. In all four equations, L_2 can be found using Eq. 2.33. [10][21]

$$\frac{\partial[\rho_m C_m T_m(x, t)]}{\partial t} + \tau_0 \frac{\partial^2[\rho_m C_m T_m(x, t)]}{\partial t^2} = \frac{\partial}{\partial x} \left(k_m \frac{\partial T_m(x, t)}{\partial x} \right) + Q_m(x, t) \quad (2.29)$$

$$k_m \left. \frac{\partial T_m(x, t)}{\partial x} \right|_{x=L_2} = \sigma \varepsilon [T_m(L_2, t)]^4 + \dot{m} C_m T_m(L_2, t) \quad (2.30)$$

$$\frac{\partial[\rho_s C_s T_s(x, t)]}{\partial t} + \tau_{0s} \frac{\partial^2[\rho_s C_s T_s(x, t)]}{\partial t^2} = \frac{\partial}{\partial x} \left(k_s \frac{\partial T_s(x, t)}{\partial x} \right) \quad (2.31)$$

$$k_s \left. \frac{\partial T_s(x, t)}{\partial x} \right|_{x=L_2} = \sigma \varepsilon [T_s(L_2, t)]^4 \quad (2.32)$$

$$L_1 = L - \Delta L \quad (2.33)$$

2.4 Modified Electro-Mechanical Model

After the ablation model is compiled and solved it is possible to move forward with the analysis and implementation of the modified electro-mechanical model part of the MEMTA model. If an integration of \dot{m} from Eq. 2.23 is performed over the pulse time it is possible to derive the cumulative ablation mass, $m(t)$ and apply it to this numerical method. In order to proceed with the numerical analysis involved in this model, some other assumptions must be made about the electro-mechanical properties of the μ PPT. In this case, it must be assumed that the circuit, shown in Fig. 2.4 below, is an LCR circuit that functions as an electromechanical device that interacts with a dynamic system. [22] The thruster is also assumed to be ideal and stable, while the thrust producing arc discharge ablation should be assumed cause full ionization. Lastly, as previously mentioned, the thrust force will be the sum of the gas dynamic and Lorentz forces.

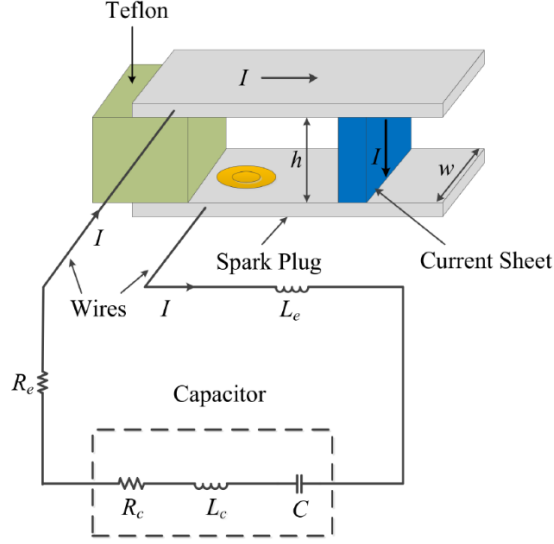


Figure 2.4 - μ PPT model and LCR circuit schematic [10]

By applying Kirchhoff's voltage law, it is possible to describe the dynamics of the LCR circuit that is shown above in Fig. 2.4. When this is done, the discharge circuit loop can be expressed in terms of the loop's total voltage $V(t)$ in Eq. 2.34, where $I(t)$ is the time-based loop current, R_T is the sum of the loop's resistance, and L_T is the sum of the loop's self-inductance. [10]

$$V(t) = I(t)R_T + \frac{d}{dt}[L_T I(t)] \quad (2.34)$$

The sum of the resistance R_T of the circuit loop for a μ PPT can be expressed using Eq. 2.35, where R_c , R_e , R_{pe} and R_p are the capacitors, leads and wires, plate electrodes and plasmas resistances, respectively. The sum of the self-inductance L_T of the circuit loop for a μ PPT can be expressed using Eq. 2.36, where L_c , L_e and L_{pe} are the capacitors, leads and wires, and plate electrodes self-inductances, respectively. [10][21]

$$R_T = R_c + R_e + R_{pe} + R_p \quad (2.35)$$

$$L_T = L_c + L_e + L_{pe} \quad (2.36)$$

The plasma resistance R_p can be solved using the expression in Eq. 2.37, where T_e is the electron temperature, n_e is the electron number by volume and t' is the time of a single pulse. [21][22]

$$R_p = 8.08 \frac{h}{wT_e^{\frac{3}{4}}} \sqrt{\frac{\mu_0 \ln \left[1.24 \times 10^7 \left(\frac{T_e^3}{n_e} \right)^{\frac{1}{2}} \right]}{t'}} \quad (2.37)$$

Next, in order to model the motion of the current sheet (seen in Fig. 2.4) the motion equation can be worked to form the expression shown below in Eq. 2.38 (which incorporates the two forces into it), where $\dot{x}(t)$ is the velocity of the current sheet away from the ablation surface and $\ddot{x}(t)$ is the acceleration of the current sheet away from the ablation surface. The cumulative ablation mass $m(t)$ can also be derived using Eq. 2.39, where $m(t_0)$ is the total accumulated ablation mass at the last time step and $\dot{m}(t)$ is the cumulative ablation mass flow rate. [21]

$$\frac{d}{dx} [m(t)\dot{x}(t)] = \dot{m}(t)\dot{x}(t) + m(t)\ddot{x}(t) = F_L + F_A \quad (2.38)$$

$$m(t) = m(t_0) + \dot{m}(t)dt \quad (2.39)$$

Based on the conditions of this μ PPT model, it is possible to derive applicable equations for the Lorentz force and the gas dynamic force from Eq. 2.3 and Eq. 2.4. The new MEMTA model Lorentz force and gas dynamic force equations are expressed below in Eq. (2.40) and Eq. (2.41), respectively. Using Eq. 2.42, it is also possible to define the electrode plate self-inductance during a single pulse, L'_{pe} . [10][21]

$$F_L = \frac{1}{2} L'_{pe} [I(t)]^2 \quad (2.40)$$

$$F_A = hwn_e\sigma T_e \quad (2.41)$$

$$L'_{pe} = \frac{\mu_0}{\pi} \left[\frac{3}{2} + \ln \left(\frac{h}{w+d} \right) \right] \quad (2.42)$$

By using Eq. (2.40) and (2.41) it is possible to modify Eq. (2.43) in this expression:

$$\frac{d}{dx} [m(t)\dot{x}(t)] = \dot{m}(t)\dot{x}(t) + m(t)\ddot{x}(t) = \frac{\mu_0}{2\pi} \left[\frac{3}{2} + \ln \left(\frac{h}{w+d} \right) \right] + hwn_e\sigma T_e \quad (2.43)$$

When placed all together, the governing Equations (2.43), (2.37) and (2.34) form the completed form of the modified electromechanical model; the second part of the MEMTA μ PPT model. Solving for these equations it is possible to modify the performance parameters mentioned in previously in section 2.1. On this basis, the specific impulse, impulse bit, thrust efficiency and thrust-to-power ratio in their MEMTA model forms are expressed in Equations (2.44), (2.45), (2.46) and (2.47), respectively. In these, the term E' represents the capacitor discharge energy per pulse. [10][21][22]

$$I_{sp} = \frac{I_{bit}}{m_{bit}g} = \frac{\dot{x}(t')}{g} \quad (2.44)$$

$$I_{bit} = \frac{\mu_0}{2\pi} \left[\frac{3}{2} + \ln \left(\frac{h}{w+d} \right) \right] \int_0^{t'} [I(t)]^2 dt + hwn_e\sigma T_e t' \quad (2.45)$$

$$\eta = g \frac{I_{sp} I_{bit}}{2E'} \quad (2.46)$$

$$\frac{T}{P} = \frac{I_{bit}}{E'} \quad (2.47)$$

3 Pulsed Plasma Thruster Performance Analysis

An analysis of equations 2.40, 2.41, 2.42 and 2.43, derived from the MEMTA model, reveals that the characteristics of the individual components and their effect on the entire system makes a significant difference on the performance qualities of a μ PPT. For the electrodes, their gap distance h , thickness d and width w , play a fundamental role in deriving the impulse bit which is needed to find the specific impulse, overall efficiency, and the thrust-to-power ratio. The power processing unit (PPU) introduces an energy per pulse E' to the system by charging the capacitor and pulsing the spark plug which induces a current $I(t)$ across the propellant surface between the electrodes. The propellants chemical properties contribute to the mechanics of the ablation process and can be measured using the electron temperature T_e and number n_e of the ablated propellant. Both of these components also play a fundamental role in deriving the I_{bit} . Thus, it is possible to vary the performance of a μ PPT by varying the parameters of each component. To do this appropriately, an analysis and trade study of μ PPT and standard PPT models, both flight heritage and test article, must be done to compute the dependencies of performance on component parameters.

3.1 Pulsed Plasma Thruster Selection and Background

The literature available for μ PPTs is growing but the vast majority of performance data that can be found exists for test articles alone. As of the year 2020, due to the relatively recent emergence of the standard model for CubeSats, developed by engineers and students at California Polytechnic Institute, there are very few μ PPTs with flight heritage. This presents a problem; it is now much harder to compile a comprehensive data set of flight heritage μ PPT performance characteristics. To remedy this issue, the scope of the analysis for this chapter was expanded so that standard PPTs and test article μ PPTs were eligible based on a range of acceptable performance qualities. The qualifying range of performance that makes a PPT model eligible for this analysis, based on the available literature, is an I_{sp} of 300-1000 seconds and an I_{bit} of 20-100 μ N-s [15][23][24][25][26][27]. This section is a study of the performance characteristics of seven of these eligible PPTs.

The first PPT chosen for this analysis, the TMIT-PPT, is a PPT designed for SmallSat applications by engineers and students at Tokyo Metropolitan Institute of Technology (TMIT). It was developed to be the primary long-term propulsion system on the μ -Lab Sat II. While this PPT was not designed to be flown on a CubeSat class spacecraft, its performance qualities still qualify it for this analysis. Compared to other PPT flown on spacecraft of a similar class, TMIT-PPT stands out as having the lowest I_{bit} and the lowest discharge energy, as seen in Fig. 3.1 below. These performance qualities exist on the outer bounds of the range of acceptable values that were previously described as eligible for this comparative analysis. Understanding the performance of larger eligible PPT, like this one, will allow for this analysis to show how PPT performance varies during the transition from standard sized PPT to μ PPT, referred to as the miniaturization process. [15]

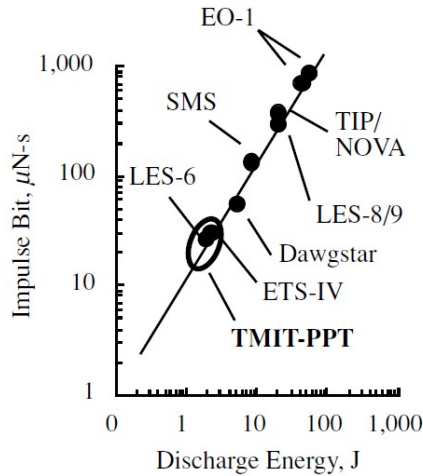


Figure 3.1 - TMIT-PPT and heritage PPT performance [15]

The next PPT chosen for this analysis is the Pulsed Plasma thruster for CubeSat applications (PPTCUP) developed by engineers at Mars Space Ltd, Clyde Space Ltd and the University of Southampton. It was designed to perform small orbit changes for drag compensation, formation maneuvers, and end-of-life deorbiting for nanosatellites. The data used for this analysis is based on a performance analysis of its breech-fed configuration test article. This test article, shown in its assembled configuration below in Fig. 3.2, was designed to produce a discharge energy of 5J and operate at a pulse voltage V_0 of 1700V. [24]

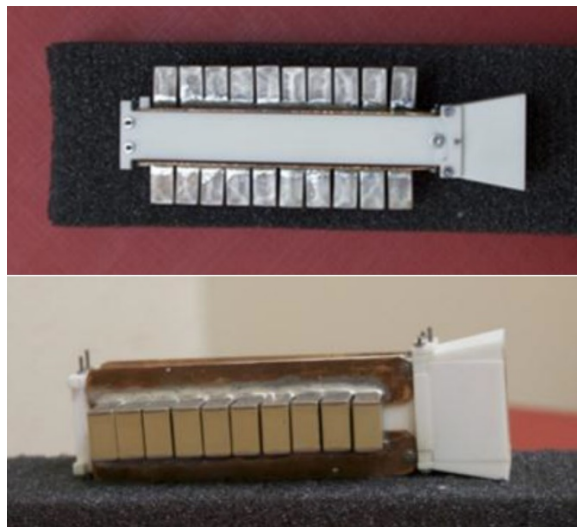


Figure 3.2 - Assembled breech-fed PPTCUP [24]

The third PPT chosen for this analysis is the side-fed configuration of the PPTCUP designed, built and tested by the same groups referenced in the previous eligible PPT. Due to its increased performance qualities over the breech-fed configuration, this PPT was chosen for extended testing and iteration. Shown below in Fig. 3.3, the side fed PPTCUP was designed to function as the primary propulsion system on a 3U CubeSat. As such, each component was designed to fit inside a 1/3U casing. This casing was designed to satisfy CubeSat design requirements and restraints, which dictate that the casing maintains a 100 mm × 100 mm outer dimension and the electronic

interface satisfy the PC104 interface design protocol. The next figure, Fig. 3.4, shows a representational sketch of the side-fed propellant configuration for this μ PPT. [23]

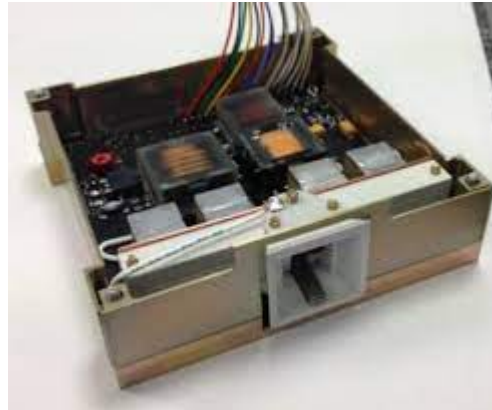


Figure 3.3 - Side-fed PPTCUP

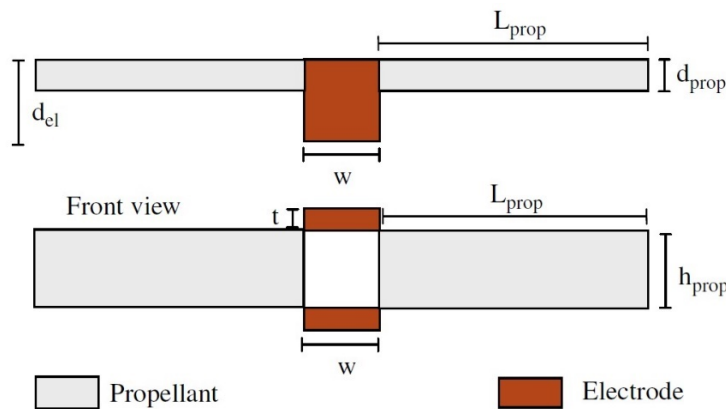


Figure 3.4 - Sketch of the side-fed PPTCUP electrode and propellant configuration

The fourth μ PPT chosen for this analysis is the Busek BmP-220 designed and built by Busek Inc, a Space Propulsion and Systems company. It is the matured iteration of the previously named MPACS (Micro Propulsion Attitude Control System) PPT which gained flight heritage on the FalconSat-3 mission. This PPT, shown in Fig. 3.5 below, is classified by Busek as a “multi-thruster,” a designation given based on its operational mechanics. It is designed with multiple cylindrical discharge chambers or “emitters” that can each be selected as the primary discharge chamber. The inclusion of multiple emitters functionally increases the operational repetition rate, which directly correlates to the pulse frequency (Hz). The average PPT has an operational repetition rate of 1-2 Hz but the Busek BmP-220 can operate at up to 7 Hz due to its multi-thruster design. For the sake of this report a repetition rate of 2 Hz was considered. [27]



Figure 3.5 - Busek BmP-220 micro-pulsed plasma thruster [27]

The fifth μ PPT chosen for this analysis is the μ PPT built for the Dawgstar nanosat, developed, and operated by Primex Aerospace Company in partnership with the University of Washington. This spacecraft, developed in 2000, was designed to be 15 kg, including its propellant, making it the first nano class satellite to fly with a propulsion system. As a result, the PPT built for this satellite would later become the first to carry the “micro” classification. It was designed for a dual-thruster configuration, shown below in Fig. 3.6, and could produce a specific impulse of 483 s while operating with an input energy of 5.2 J. The Dawgstar nanosat was equipped with 4 of these thruster-sets that could maintain the satellites 375 km orbit at an average operational power output of 3.3 W. Developmental testing of this μ PPT, provided grounds for the qualification of mica-paper/foil capacitors for voltage discharge, which would go on to become the primary capacitor choice for later μ PPTs due to their high energy density and robust design. Discussed later in this initial analysis, this thruster relied on heritage from previous standard PPT like the LES-6, and thus adopted some of the initial operating conditions such as a 28V input voltage. [29]

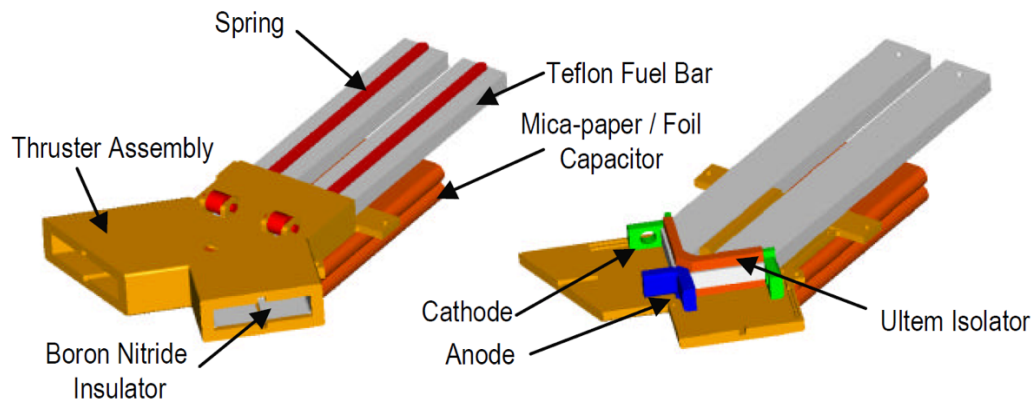


Figure 3.6 - Mechanical design of the Dawgstar μ PPT flight unit [29]

Developed and flown in 1968 on the LES-6 satellite by engineers at the Lincoln Laboratory at MIT, the sixth PPT chosen for this analysis is the LES-6 PPT. It was designed to perform station-keeping operations of the spin stabilized, synchronous LES-6. This configuration became the first pulsed plasma thruster to receive flight heritage and set multiple performance and operational benchmarks for PPTs developed in the years following its launch, including many chosen for this PPT performance analysis. Though this PPT was not designed for a nanosatellite, its performance qualities, 300 second I_{sp} and 26 μ N-s I_{bit} , place it within the bounds of eligible PPTs for this

analysis. Along with that, the historic significance among PPTs of this system means it is an appropriate benchmark to compare the effects of miniaturization on PPT performance. The thruster, shown below, in Fig. 3.7 in its flight configuration, features a pair of discharge chambers with a breech-fed propellant mechanism and parallel electrodes. Altogether, the LES-6 was equipped with 9 PPTs weighing 1.4 kg in total and requiring the expenditure of 1.85 J of energy from the satellites main system for discharge. [31]

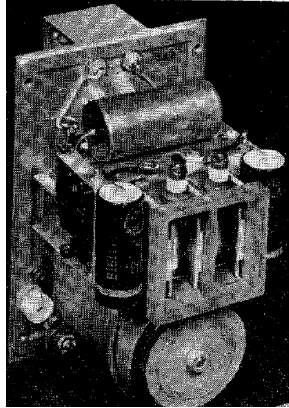


Figure 3.7 - Flight configuration of the LES-6 PPT [31]

The seventh PPT chosen for this trade analysis is the CubeSat μ PPT developed by Clyde Space Ltd, Mars Space Ltd and the University of Southampton under an ESA funded project. It was the development model of the PPTCUP mentioned previously as the second and third μ PPTs chosen for this analysis. While it has no flight heritage, the extensive number of tests performed on this μ PPT has afforded it a technology readiness level (TRL) of 4, meaning this configuration has been validated in a lab setting. Since this report involves the design of a test article μ PPT intended for a lab, it would be valuable, still, to have a lab validated μ PPT for the sake of comparison. This test article was tested at varying charge voltages ranging from 950 V to 1550 V, corresponding to discharge energies between 1 and 2 J. This μ PPT was designed to test the performance of some Commercial of the Shelf (COTS) components which were compared to the performance of custom flight qualified hardware. It was also designed to meet specific mass and size requirements based off of established CubeSat sizing requirements. Unlike other μ PPT and PPT in this trade analysis, since it is a test article, this μ PPT, shown in Fig. 3.8 below, was not built with a flight housing/enclosure. [13]

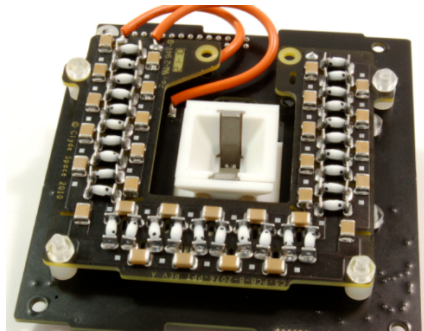


Figure 3.8 - Clyde Space CubeSat PPT test article [13]

The final μ PPT chosen for this analysis was the Dual-Axis PPT (dPPT) developed for the Aoba Velox-III (AV3) 2U CubeSat by researchers and engineers at Nanyang Technological University in Singapore. It incorporates two μ PPTs, one breech-fed and one side-fed, into a single PPT system. This allowed for a more precise thrust selection for operation and also functioned as a robust test configuration for comparison of breech-fed and side-fed μ PPTs. This was possible because both configurations are paired to the same PPU. This can be seen in the Fig. 3.9 below. Capable of 2.25 W of average operational power output and a total impulse of up to 53 Ns, this μ PPT was designed with specific mission parameters in mind. [33]

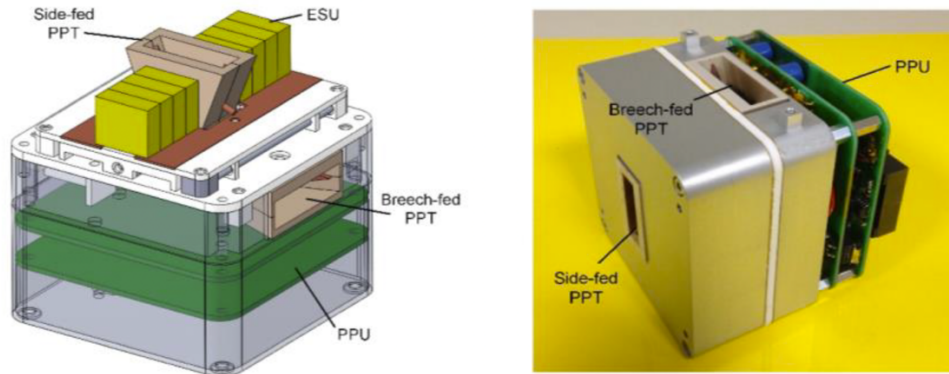


Figure 3.9 - AV3 dPPT design configuration [33]

3.2 Overall μ PPT Performance Parametric Analysis

Table 1, shown below, shows the performance data for the seven eligible PPTs. It includes each thruster's I_{sp} , I_{bit} , η , T_{sp} – or T/P , and E' (also known as the capacitor energy or pulse energy). It is also relevant to note that values denoted with an asterisk refer to terms determined through tabulation based on given information. They represent seven of the PPTs that closest fit within the predetermined parameters for this micro-pulsed plasma thruster performance analysis and subsequent design parameter selection. Each one of these PPT contains either a breech-fed propellant system or a side-fed propellant system. Based on this, it is possible to produce initial performance parameter ranges that qualify the PPT designed for this as a micro-class PPT or μ PPT. Those performance parameter ranges are:

- Specific Impulse, I_{sp} : **300-1000 s**
- Impulse Bit, I_{bit} : **20-100 μ N-s**
- Propulsive (Thrust) Efficiency, η : **2-7%**
- Specific Thrust or Thrust-to-Power Ratio, T/P : **5-20 μ N/W**
- Discharge Energy, E' : **1.2-6 J**

Table 3.1 - Performance qualities of eligible PPT and μ PPT

PPT Type	I_{sp} (s)	I_{bit} (μ N-s)	η (%)	T/P (μ N/W)	m_{bit} (μ g) *	E' (J)	TRL
TMIT-PPT [15]	960	21.5	3.06	6.5	2.29	3.3	4
Breech-fed PPTCUP [24]	640	90	5.6	18	14.35	5	5*
Side-fed PPTCUP [25]	655	40	6.4	20	6.23	2	5*
Busek BmP-220 [27]	536	20	4.2*	16*	3.81	1.3*	6
Dawgstar μ PPT [30]	483	56.1	2.5	11	11.85	5.23	6
LES 6 [30]	300	26	2	17	8.84	1.9	9
CubeSat μ PPT [13]	585	29	4.48	16.8	5.06	1.71	4
AV3 Dual-Axis PPT [33]	525	22.5	2.6*	10*	4.35	2.25	4

These parameter ranges, while vast and non-specific individually, are valuable when analyzed together since they are a representation of trends in performance for PPTs of this specific classification. While the list of PPTs that have been developed includes many dozen models, PPTs that are parallel rail electrode, spring-fed PTFE and designed for nanosatellites, like the one considered for this experimental design, can essentially be narrowed down to the list shown above. This means that, though this list is short, it is quite exhaustive considering the specificity of this analysis and the relative novelty of μ PPT research.

Based on the accumulated performance values found in Table 1, it's possible to perform an overall analysis of μ PPT performance in qualified models such that trends in performance can be identified. According to research performed by one of the earliest PPT engineers, William J. Guman, and preliminary performance studies performed for the PPTCUP thrusters, the relationship between the impulse bit and discharge is fundamental in understanding the trends in PPT performance [24][32]. The ratio of these values is the specific thrust, which is also considered the thrust-to-power ratio. There exists no common nomenclature for this term in available literature, so for the purposes of this report the specific thrust will be denoted as T_{sp} .

A look into the performance trends in all forms of PPTs shows that discharge energy is an effect predictor of I_{bit} , m_{bit} and, conditionally, I_{sp} [30][32]. The reason I_{sp} cannot always be estimated by analyzing trends in energy is because the sample range for discharge energies must be wide (at least from 0-100 J) to produce a relevant trendline. At low discharge energies the correlation between I_{sp} and E' becomes progressively less evident. Since μ PPTs operate at values of E' lower than 6 J it is much more difficult to produce a reliable trendline to estimate performance. Proof of this can be found in the survey of PPTs previously cited, where performance data from dozens of PPTs was compiled and analyzed [30]. Fig. 3.10, below, features a plot from that report which shows the relation between I_{sp} and E' at values of up to 10,000 J. At values lower than 10 J, the apparent linear correlation is much harder to identify.

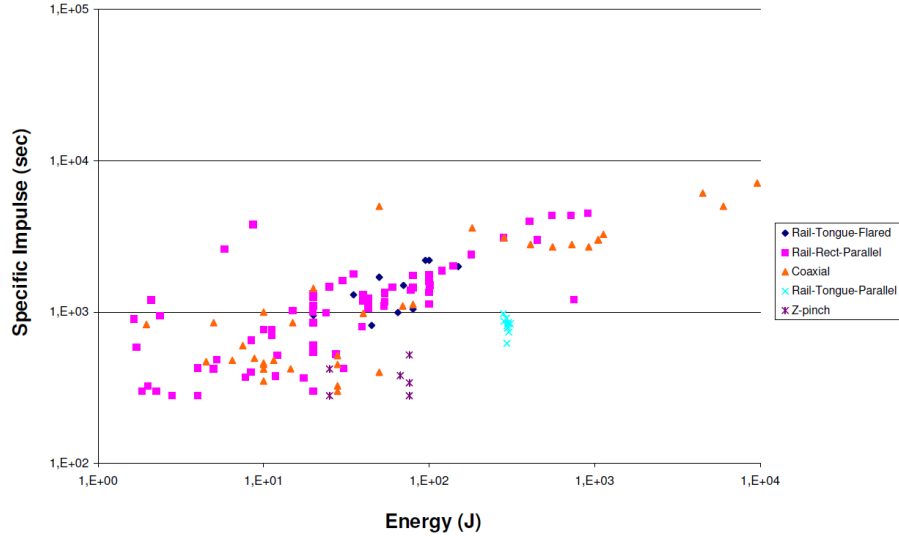


Figure 3.10 - I_{sp} and E' performance comparison of worldwide PPTs [30]

As for I_{bit} and m_{bit} , their correlation with E' is far more apparent. Fig. 3.11, below, shows the I_{bit} versus E' plot produced by researchers at Clyde Space from the experimental results of the CubeSat μ PPT performance tests. The plot shows a positive linear correlation that is consistent with trends seen in larger sample sizes. The slope of this line, represented by Eq. 3.1, is representative of the specific thrust, T_{sp} . For the design of this specific μ PPT, a baseline of 10-15 μ N-s/J was considered, with 10 μ N-s/J representing a non-optimal case and 15 μ N-s/J representing an optimal case [24]. In a similar analysis of T_{sp} , based on William Guman's work, the least-square interpolation of previous experimental PPTs ranging between 1 and 460 Joules, yield a T_{sp} of 20.7 μ N-s/J. When that discharge energy range of 5-to-50 J was considered, this value dropped to 14 μ N-s/J. Since this analysis is only considering PPT's that have discharge energies below 5 J, it must follow that the T_{sp} should be lower than 14 based on the apparent trend [32]. Due to the similarities in scope of the Clyde Space CubeSat μ PPT and the μ PPT being considered in this design report, it is appropriate to apply this same T_{sp} baseline and assumptions to the latter.

$$T_{sp} = \frac{I_{bit}}{E'} \quad (3.1)$$

When the values of I_{bit} and E' from Table 1 are plotted it produces the graph shown in Fig. 3.12 below. The linear regression function of this set of points, also shown, produces a slope, and subsequent T_{sp} value, of 12.65. The value is almost exactly in between the optimal and non-optimal cases. Though this is "not optimal," it sits within an acceptable range and qualifies as an appropriate initial design value for T_{sp} as it follows the downward trend of values for this term with lower ranges of E' . Along with this term, an acceptable range for the discharge energy must be chosen in order to conduct a trade analysis of I_{bit} , m_{bit} and I_{sp} performance.

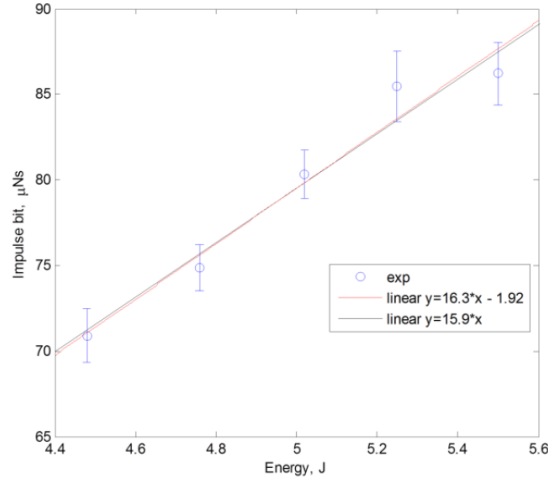


Figure 3.11 - Clyde Space CubeSat PPT comparison of impulse bit vs. discharge energy [24]

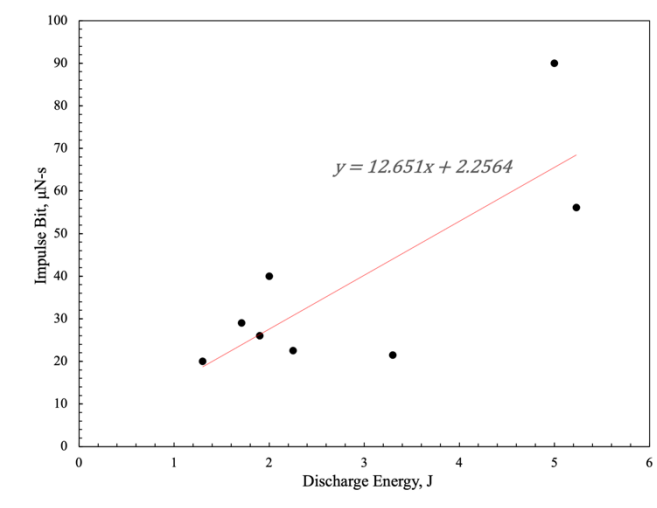


Figure 3.12 - μPPT trade comparison of impulse bit vs. discharge energy

The resulting regression function becomes:

$$I_{bit} = 12.651E' + 2.2564 \quad (3.2)$$

Using the Eq. 3.2 produced from the plot above, it is possible to obtain a range of initial values for I_{bit} for this analysis. To obtain a range of initial values for m_{bit} and I_{sp} , regression function for the correlation plot of m_{bit} and E' is needed. This and corresponding plot are shown below in Fig. 3.13 and Eq. 3.3 is the resulting regression plot. If m_{bit} and I_{bit} are assumed to have a linear proportionality, the I_{sp} could also maintain a roughly constant value or, according to other performance studies, show no correlation with E' [32]. This is further proof of the lack of consensus on the correlation of I_{sp} and E' .

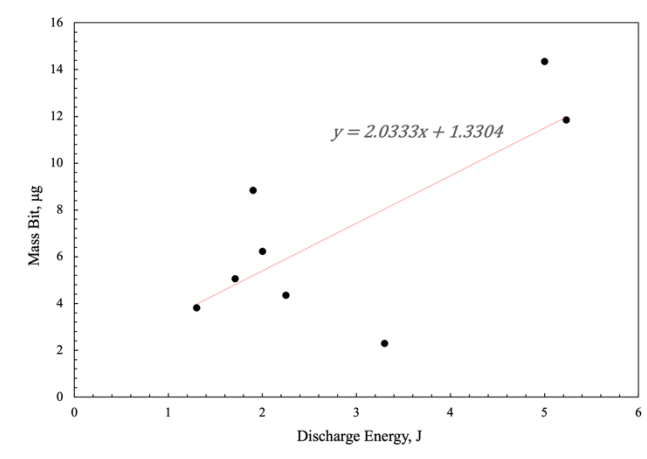


Figure 3.13 - μ PPT Trade comparison of mass bit vs. discharge energy

The regression function becomes:

$$m_{bit} = 2.0333E' + 1.3304 \quad (3.3)$$

Since the I_{sp}/E' correlation plot produces unreliable trends at low energies, another approximation method for I_{sp} must be implemented. Based on research performed by Paolo Gessini and Giorgio Paccani, I_{sp} , I_{bit} and E' can be correlated using the function shown below in Eq. 3.4, which can be derived from the least-square interpolation of the available data. The terms α and β , are coefficients that can be found from the regression function produced from the resulting plot.

$$I_{bit}I_{sp} = \alpha E'^{\beta} \quad (3.4)$$

From the available data, that plot that is produced is:

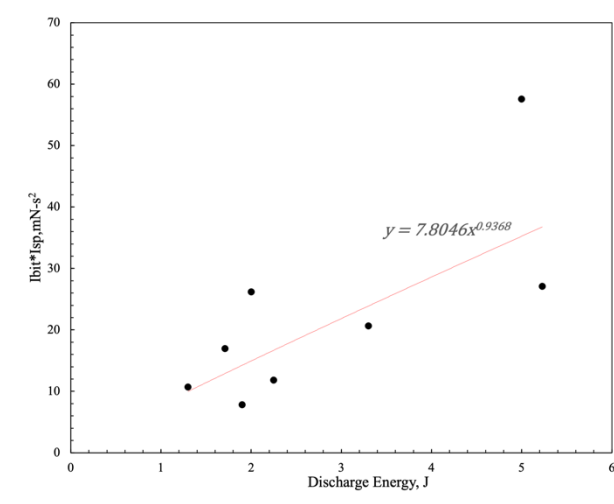


Figure 3.14 - μ PPT trade comparison of impulse bit, specific impulse, and discharge energy

This results in a regression plot in the form of the Eq. 3.4 where the coefficients α and β gain the values 7.8046 and 0.9368, respectively, in Eq. 3.5 below:

$$I_{bit}I_{sp} = 7.8046E'^{0.9368} \quad (3.5)$$

Solving for the I_{sp} in Eq. 3.5 produces the plot shown below in Fig. 3.15.

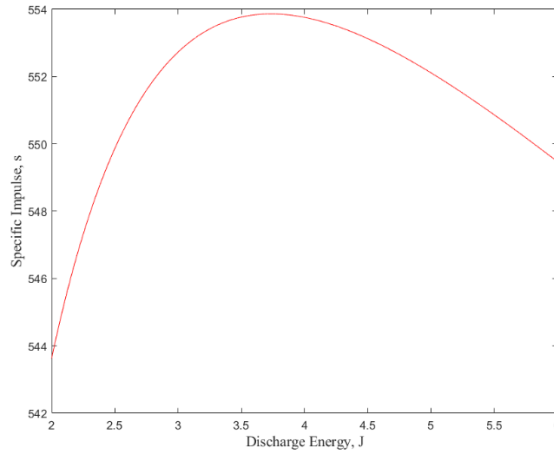


Figure 3.15 - Specific impulse trend as a function of impulse bit

Ultimately, the range of E' values that was considered for this was 2-6 J. This range was chosen for three reasons. The first is that the proportionality displayed in Eq. 1.1 paired with Eq. 3.1, show that low propellant surface areas correspond to low T_{sp} values, which corresponds with a higher required E' value. The second reason is that some PPTs with low E' values can still produce higher relative efficiencies. As a result, the range includes low and high values while excluding the lowest. The final and most relevant reason is that the available research indicates that PPTs of the parallel rail configuration, hold a “micro” classification at these discharge energy levels.

Using this range of E' values and the regression functions from Fig. 3.12, Fig. 3.13 and Fig. 3.14, it's possible to update the initial performance parameter ranges to accommodate these first performance approximations:

- Specific Impulse, I_{sp} : **400-700 s**
- Impulse Bit, I_{bit} : **29-78 μ N-s**
- Propulsive (Thrust) Efficiency, η : **2-7%**
- Specific Thrust or Thrust-to-Power Ratio, T/P : **12-15 μ N/W**
- Discharge Energy, E' : **2-6 J**

Over the next few sections of this report, individual trade analyses on each individual major component will be performed to refine these values down to higher fidelity performance estimates.

3.3 Capacitor Characteristics and Parametric Analysis

When considering the design, development, and optimization of a μ PPT it is vital to first consider the characteristics of the capacitor or, the likely capacitor bank. It is quite possibly the most consequential single component of the entire thruster. This is due to its direct correlation with the discharge energy, which is most referred to as the capacitor discharge energy. Evidence of this correlation can be seen Eq. 2.4, discussed previously in chapter 2 of this report. This equation shows a direct proportionality between the capacitance and the discharge energy. Later in this chapter this equation will be utilized to establish an acceptable design range for the capacitance required for this design.

3.3.1 Capacitor Bank Design Considerations and Characteristics

The capacitor bank in a μ PPT functions as the primary voltage source for the pulse since it is the most effective way to pulse high voltages on an extremely short timescale. In general capacitors rely on an internal electric field that propagates between pairs of conducting plates to store energy. The stored energy in this electric field induces a potential difference which, in this case, will be equivalent to the input voltage V_0 . This process is the first of two phases, the charging phase. Based on the properties of the capacitor, namely its capacitance C , and the properties of the circuit it's possible to charge a capacitor within a specified charge time t_c . This is vital to the operation of PPTs since pulse frequencies can be as high as 3 Hz for single chamber PPTs. Therefore, it is imperative that the capacitor be able to charge and discharge in a fraction of a second. The second phase of capacitor operation is the discharge phase, which, like the charge phase, can be engineered to last a specified discharge time t' . For the μ PPT being design in this report, the capacitance, charge time, discharge time and circuit properties will function as critical design factors.

Another design consideration for the capacitors in this μ PPT is the exact amount needed for operation. Due to the high input voltages required to produce one pulse, HV (high voltage) capacitors must be used, and these capacitors tend to have low capacitances ($< 0.2 \mu\text{F}$). As such, most μ PPT developers will connect multiple capacitors in parallel to increase the overall capacitance. This method relies on the total equivalent circuit capacitance formula for capacitors in parallel, shown below in Eq. 3.6, that simply states that the total equivalent capacitance is the sum of the capacitances of each capacitor that is connected in parallel [34]. In most cases, this parallel-connected grouping of capacitors is referred to as the capacitor bank.

$$C_T = C_1 + C_2 + C_3 \cdots + C_n \quad (3.6)$$

In general, there are three main types of capacitors that can be found in any type of capacitor bank, for any application. While it's possible to delineate a more comprehensive list of capacitors from all known uses, it's still useful, in this case, to classify most commonly used capacitors into three types. These three types are:

1. Ceramic capacitors
2. Electrolytic capacitors

3. Film/Paper capacitors

Ceramic capacitors are capacitors that are composed of layered ceramic material with a conductive material sandwiched in between each layer. Many ceramic materials have a high permittivity, and this enables physically small capacitors to have high voltage ratings, or maximum acceptable voltages, and high operational frequencies. In contrast, electrolytic capacitors contain layers of aluminum foil in between layers of an absorbent material, like paper, impregnated with an electrolyte, such as ammonium borate. The foil functions as the dielectric for the capacitor and ultimately forms an aluminum oxide layer within the capacitor. Due to the resulting aluminum oxide layers, these capacitors can only operate within a DC circuit and cannot operate in a reversed polarity. If this is not done the oxide layer will be permanently damaged. Lastly, film/paper capacitors are capacitors where a plastic polymer or metal foil film functions as the dielectric within the capacitor and is sandwiched in between layers of paper bound tightly in a cylindrical or rectangular configuration. These capacitors are known for their high voltage ratings that can be as high as 150 kV. Film capacitors in particular have a high reliability, can function in high temperatures and boast a high service life. [34]

In light of the capabilities of each of the different types of capacitors available, it's likely that the most suitable capacitors for this μ PPT design are ceramic and film capacitors. This is due to the fact that electrolytic capacitors cannot operate in a circuit of reverse polarity. While the nominal voltage of a PPT discharge circuit is positive, for a moment during the pulse, the voltage drops below zero. This will lead to the rapid deterioration of the capacitor. As a result, the design constraints must take into consideration the operational capabilities and limits of ceramic and film capacitors. Table 2, below, shows the operational standards that must be considered for these types of capacitors.

Table 3.2 - Capacitor type properties

Capacitor Type	Max. Voltage Rating, kV	Operational Temp, °C	Capacitance Range
Ceramic	50	-55 ~ 260	1 nF ~ 1 μ F
Film	10	-55 ~ 150	1 nF ~ 30 μ F
Paper/Polymer	150	-55 ~ 150	10 μ F ~ 1 mF

The above listed properties along with the design constraints and capacitor parametric analysis will dictate the performance of the capacitor during operation. Along with this, performance properties of capacitors during the charge and discharge phases will also determine how the capacitor will function. The functions that govern these two phases of operation are based on two separate assumptions, one for each phase.

For the charge phase of capacitor operation, it is appropriate to assume that the circuit is a DC C-R circuit meaning that its components can be summed up as a capacitor and resistor in series with a power source providing a direct, constant current [34]. This represents the left-hand side (LHS) of the circuit shown in Fig. 3.16. This diagram is a simplified version of a PPT circuit diagram, which will be further expounded upon in chapter 3.4. For now, this diagram shows that, physically, the charge and discharge phases of capacitor operation for a PPT can be split into left-hand side and right-hand side current loops (RHS), respectively. Though this is not the

conventional circuit nomenclature, in this case, it is useful due to the distinct differences in the current loop properties on the left and right of the capacitor bank.

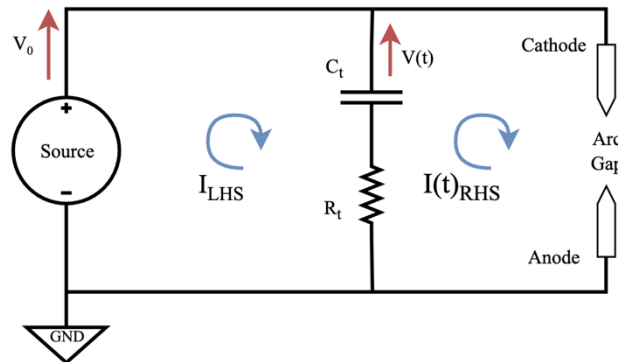


Figure 3.16 - PPT circuit diagram w/ current loops

During the charging phase, the voltage stored across the capacitor grows while the current and voltage across the resistor – or sum of all resistive elements – decays. The exponential growth curve that depicts the capacitor voltage growth and the exponential decay curve that depicts the resistor voltage and current decay are both characterized by a curve that settles at a specific value or zero. These are shown below in Fig. 3.17. In both cases, the behavior of the curves can be represented using the time constant τ , which is defined as the time taken for a transient to reach its final state if the initial rate of change is maintained [34]. This term, τ , is the product of the capacitance and the resistance of the circuit. In the case of a PPT, it refers to the total capacitance of the capacitor bank and the total circuit resistance, respectively, as can be seen in Eq. 3.6 below. This term is measured in seconds. [34]

$$\tau = C_t R_t \quad (3.5)$$

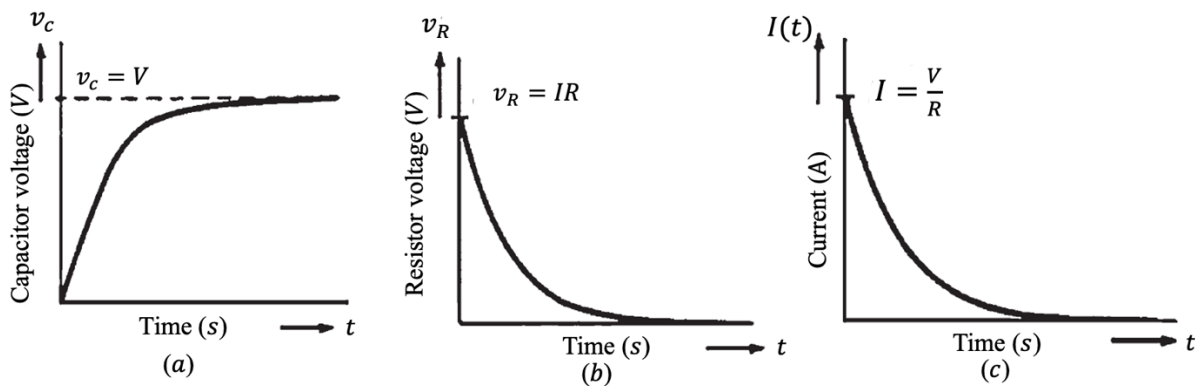


Figure 3.17 - Capacitor and resistance voltage and current transient curves for a charging capacitor

The transient curves shown in Fig. 3.17, result in Eq. 3.7, 3.8, and 3.9, that are the numerical representations of their differential solutions [34]. These are shown below:

$$v_c = V_0(1 - e^{-t/\tau}) \quad (3.7)$$

$$v_R = V_0 e^{-t/\tau} \quad (3.8)$$

$$i = I_0 e^{-t/\tau} \quad (3.9)$$

After an amount of time equal to one time constant, the value of the exponential growth capacitance voltage transient is 63.2% of the steady state voltage V_0 . For the resistance voltage and current exponential decay curves their transients are 36.8% of their steady state values – V_0 and I_0 – when the amount of time equals one time constant. The logic follows that when the capacitor voltage v_C reaches V_0 , and when the resistor voltage v_R and i reach zero, the time elapsed is equal to 5 times the time constant. This relationship can be seen below in Eq. 3.10:

$$t_{ss} = 5\tau_{ch} \quad (3.10)$$

For a PPT, t_{ss} is a required parameter for efficient operation. This means it is possible to determine the systems time constant by setting a desired value for the total time for the capacitance voltage to reach steady state values. Since the capacitors must charge and discharge at a rate of 1 Hz and discharges can last only microseconds for PPTs, it's possible to set the required t_{ss} for a PPT to charge to 0.5 seconds or 500 milli-seconds. At this value, the required time constant for operation is 100 milli-seconds. Once the capacitance to chosen, it is possible to determine the required resistance to complete the LHS charging circuit.

During discharge, the circuit, as was mentioned in chapter 2, behaves as an LRC circuit. For the sake of simplicity in this initial analysis and to set initial parameters, the capacitors time constant will still be characterized by Eq. 3.6 like in an RC circuit. This allows for a quick estimation of discharge time t' , before performing a more in-depth analysis on the modelled performance of the LRC circuit. In this phase, the capacitor voltage and current experience an exponential decay in their transients until they reach zero. In this case, like with the charge phase, the time to discharge to zero is five times the time constant, as is seen in Eq. 3.11 below. Due to the discrepancy between this discharge time estimate and the actual discharge time of the LRC circuit, the estimated discharge time will be denoted as t_e' .

$$t_e' = 5\tau_{dis} \quad (3.11)$$

3.3.2 Capacitor Parametric Analysis

As previously mentioned, utilizing Eq. 2.4 makes it possible to set a design capacitance for this μ PPT by setting a desired discharge energy. Using the discharge energy range of 2-6 J pulled from the initial performance parameter analysis performed in chapter 3.2, it's also possible to set a range of capacitance values for this design. Before that can be done, a discharge voltage V_0 must also be chosen. To do this, in this section, a parametric analysis will be performed to assess the capabilities of heritage PPTs and μ PPTs. Table 3, below, shows the capacitor performance characteristics of these PPTs. The section labelled C refers to the total capacitance of the PPTs capacitors, the section labelled n refers to the total amount of capacitors in the capacitor bank and the section labelled C_1 refers to the capacitance of each individual capacitor in the bank.

Table 3.3 - Capacitor performance parameters

PPT Type	C (μF)	n	C_1 (μF)	E' (J)	V_0 (V)	TRL
TMIT-PPT [15]	2.95	3	1.0	3.3	1500	4
Breech-fed PPTCUP [24]	4.0	20	0.2	5	1700	5*
Side-fed PPTCUP [25]	1.6	8	0.2	2	1720	5*
Busek BmP-220 [27]	--	--	--	1.3*	--	6
Dawgstar μPPT [30]	5.0	1	5.0	5.23	1450	6
LES 6 [30]	8.0	4	2.0	1.9	1360	9
CubeSat μPPT [13]	2.5	10	1.0	1.71	1200	4
AV3 Dual-Axis PPT [33]	2.0	8	0.25	2.25	1500	4

Based on the data above, it's possible to identify trends in performance parameters for μPPTs within the energy range considered for this design. One such trend is the tendency for the discharge voltage to be close to 1500 volts and another is that the capacitance tends to be less than 4.0 microfarads. These trends are plotted below in Fig. 3.18.

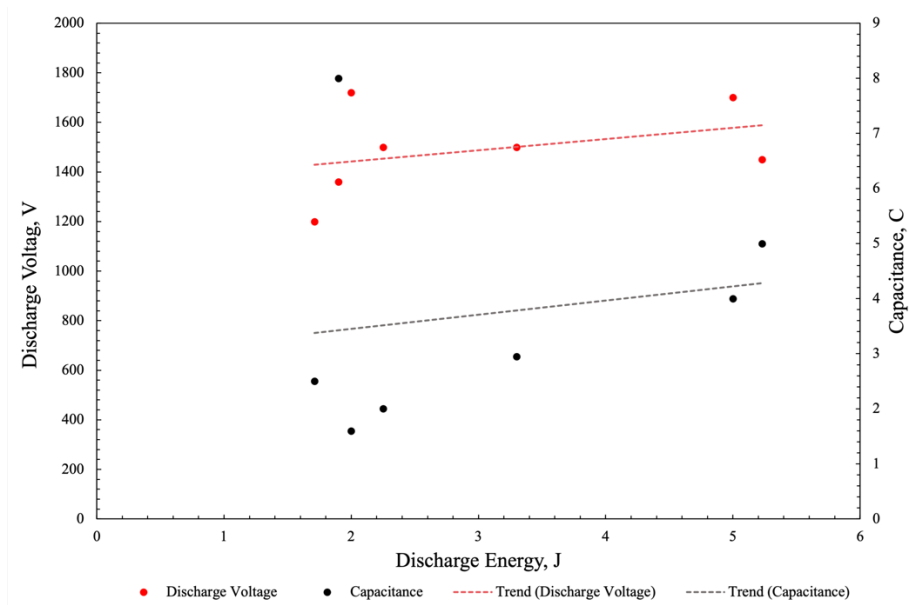


Figure 3.18 - Capacitance & discharge voltage v. discharge energy of chosen μPPTs

The trendlines shown in Fig. 3.18, while not precise enough to serve as any form of predictive function, show how there is a clear upward trend in required capacitance and discharge voltage as the discharge energy increases. This positive correlation accurately tracks with the positive

proportionality between capacitance and discharge energy found in Eq. 2.4. While there seems to be a positive linear correlation between discharge voltage and discharge energy, for heritage PPTs, it seems there is a higher tendency for it to gravitate around certain fixed values. As such, this analysis will look at capacitor performances at 1200, 1500 and 1700 volts. Using this and Eq. 3.12 below, which is Eq. 2.4 solved for capacitance, it's possible to generate a plot of the range of possible capacitance values for the viable discharge energy range determined in the previous section.

$$C = \frac{2E'}{V_0^2} \quad (3.12)$$

The plot of this function at each of the three discharge voltages is shown below in Fig. 3.19:

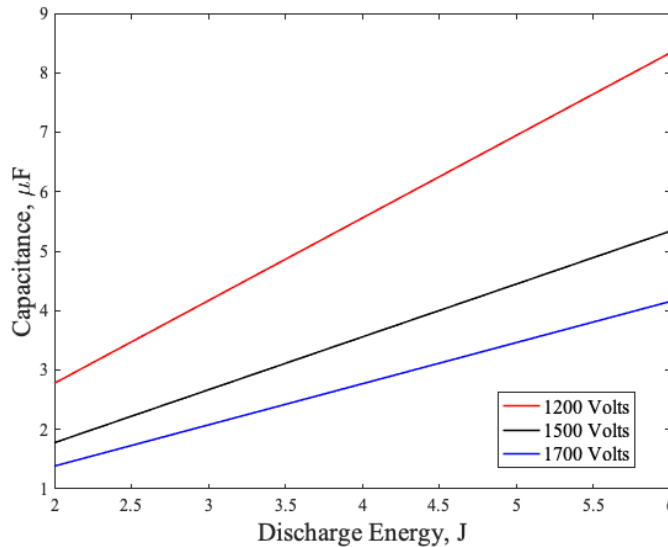


Figure 3.19 - Capacitance for three discharge voltages at various discharge energies

At lower discharge voltages, the required capacitance needed to produce the same discharge energy is higher than what would be needed for high discharge voltages. This means that at higher input voltages the required number of capacitors needed for a single capacitor bank is lower, which directly correlates to saved mass. That said, it also means that the spacecraft bus voltage must be converted to a higher voltage, which, in the case of a transformer, could result in more system mass than anticipated [34]. Due to this, a discharge voltage of 1500 V will be chosen, which also has the advantage of being the most chosen discharge voltage for PPTs and μ PPTs alike.

At this discharge voltage, the capacitances range between 1.8 and 5.3 μ F in the 2 to 6 discharge energy range. At lower energies, it makes the most sense to use a ceramic capacitor since they can weigh as little as 250 mg, even for high voltage units. Though ceramic capacitors that function at very high voltages (>1000 V) tend to not have capacitances higher than 0.2 μ F, a bank of multiple of these capacitors would likely not weigh more 5g. At high capacitances, it is likely more appropriate to use film capacitors since they can maintain high voltages (>1000 V) at capacitances as high as 4.0 μ F. This advantage comes at a cost since film capacitors can take up 10-100 times more volume than a ceramic capacitor. This must be taken into consideration when a final capacitance is chosen. [34]

3.4 Power Processing Unit Characteristics and Design Considerations

The power processing unit (PPU) in a pulsed plasma thruster refers to the sum of all the electrical components excluding the capacitor. This includes the main controller and monitoring unit, dc-dc voltage conversion system, resistors, ignition spark system and transmission lines. Each of these components introduce an inductance and resistance to the circuit that must be considered for operations, particularly those components that lie with the RHS current loop shown in Fig. 3.16. Unfortunately, the performance specification for PPU in heritage and test PPTs are rarely ever recorded. For this reason, this section will primarily focus on the characteristics and background of the overall circuit design, voltage conversion system and ignition spark system. While important, an in-depth analysis of the resistors, controlling and monitoring system, and transmission lines is out of the scope of this reports objectives.

3.4.1 Overall Circuit Characteristics and Theory

The diagram shown in Fig. 3.16, while accurately representing the high voltage discharge circuit of a PPT, does not include the entire circuit design. In most CubeSats, the entire system is powered by a 3V – 12V DC power source, so to produce 1500 volts to charge the capacitors for discharge in a PPT, there needs to a DC-DC converter that will increase the voltage exponentially. Additionally, to initiate the discharge, an arc must be produced on the exposed Teflon surface to induce the capacitor bank current to flow across the propellant face. A control unit, usually a separate processor, would activate switches to control the timing of the discharge. In total the resulting circuit would likely look like Fig. 3.20, shown below. In that diagram, the spark circuit and switches – denoted by “SW” – were included to fully represent the components needed to make a PPT operational. The DC-DC converter, otherwise known as a transformer, is also represented for the main and spark circuits.

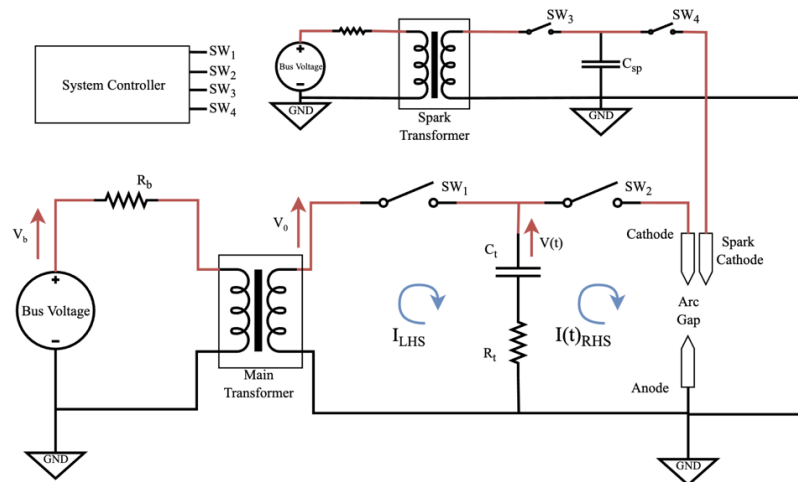


Figure 3.20 - PPT PPU full representative circuit diagram

In the figure, the ignition/spark circuit is almost identical to the main discharge circuit. This is due to the fact that this configuration gives the controller the most control over the discharge. This controller comes primarily through HV switches, labelled “SW_n” in Fig. 3.20, that are

connected to the controller. This circuit design, though still a representation and not yet complete, takes a similar approach as the one developed by the NANOSTAR Consortium that designed a PPT for nanosatellite operations. [35]

On the RHS current loop, as previously mentioned, the circuit functions as an LCR alternating current circuit. In this model, as seen in Eq. 2.34, 2.35, and 2.36 from the electromechanical component of the MEMTA model, the characteristics of the discharge current and voltage are dependent on the total resistance R_T , total inductance L_T and total capacitance C_T of the circuit. Specifically, based on research done by W. H. Guman and restated by S. J. Pottinger and M. Coletti, the discharge current can be described by Eq. 3.13 which assumes that the LCR circuit has an underdamped current response. The term ω is found using Eq. 3.14. [13][36]

$$I(t) = \frac{V_0}{\omega L_T} e^{-\frac{R}{2L}t} \sin(\omega t) \quad (3.13)$$

$$\omega = \sqrt{\frac{1}{L_T C_T} - \frac{R_T^2}{4L_T^2}} \quad (3.14)$$

Similarly, the resulting voltage curve from the discharge can be described as the underdamped function shown in Eq. 3.15, where the term δ is found using Eq. 3.16. This can be seen below:

$$V(t) = \frac{V_0}{\omega \sqrt{L_T C_T}} e^{-\frac{R}{2L}t} \sin(\omega t + \delta) \quad (3.15)$$

$$\delta = \tan^{-1} \left(\frac{4L_T}{R_T^2 C_T} - 1 \right)^{1/2} \quad (3.16)$$

In both cases (for voltage and current), the curves represent an underdamped function that at its critically damped condition of the damping ratio ζ , fulfills Eq. 3.17 shown below:

$$\zeta_{cr} = \frac{C_T R_T^2}{4L_T} = 1 \quad (3.17)$$

These equations function as the analytical method for deriving the performance qualities of the PPT designed for this report. Since it is extremely challenging to model an entire PPTs process using a single tool, the numerical performance will be a extrapolate from a heritage circuit design for μ PPTs.

3.4.2 DC-DC Conversion System

The component within the PPU that drives the voltage needed for discharge is the DC-DC convertor. In this case it will be referred to as a transformer. A transformer is a device that utilizes mutual induction to modify the voltage and current of as circuit. It does this by running the input, or primary, voltage through a coil of N_1 turns which produces an electromagnetic field (emf) within

the transformer. On the other side of the unit there is another, secondary coil of N_2 turns that supplies the output voltage. Due to the emf produced by the primary coil, a current is induced in the secondary coil. The difference in coil turns of the two coils leads to an energy difference between them and, as a result, a voltage difference. A diagram of this can be seen below in Fig. 3.21. [34]

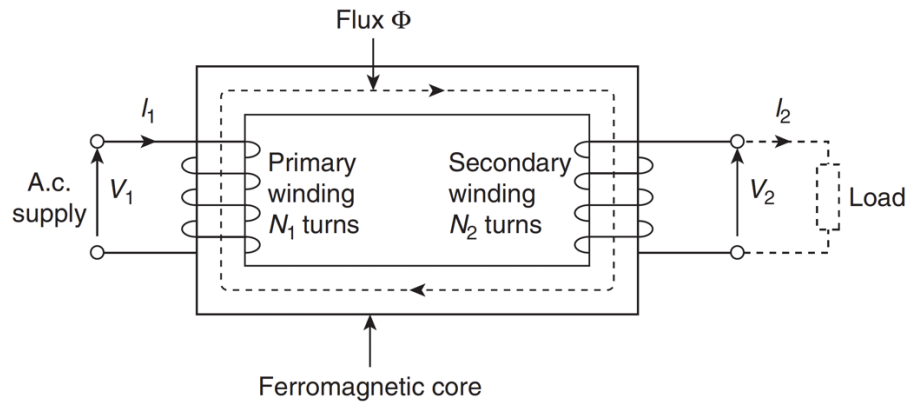


Figure 3.21 - Diagram representation of transformer operation [34]

Typically, transformers function with AC circuits but in the case of this PPT design a DC-DC transformer will be utilized. For the sake of accuracy, a real-world transformer will be chosen.

3.4.3 Ignition Spark Circuit

As shown in the full circuit diagram, the ignition spark circuit is just a slightly simpler version of the main discharge circuit. This is due to the fact that the ignition, much like the main discharge requires a high voltage arc discharge to occur across the propellant surface. The main, and most important difference is that the arc discharge produced by the ignition spark circuit is needed to force the main capacitors current to flow across the surface of the propellant leading to ablation.

The logic behind the inclusion of this circuit to the PPT architecture fully relies on an electrodynamic phenomenon called “spark gap triggering”. This phenomenon is exactly how it sounds, two electrodes with a very high potential difference between them and are not physically connected, can be electrodynamicly “triggered” to pass current through a spark gap with the help of a third, higher voltage electrode that sits in between them both. High energy devices like triggered spark gaps will utilize this effect to rapidly switch high levels of stored energy. In the case of the PPT, the trigger electrode is connected to the ignition spark circuit, which, at a high voltage, will cause an arc across the propellant surface, which will induce the main discharge to occur and cause ablation. This works because the negative side of the ignition spark circuit is wired at the anode of the main discharge circuit so that they share the same anode. Fig. 3.22, below, a simple illustration of this process. [37]

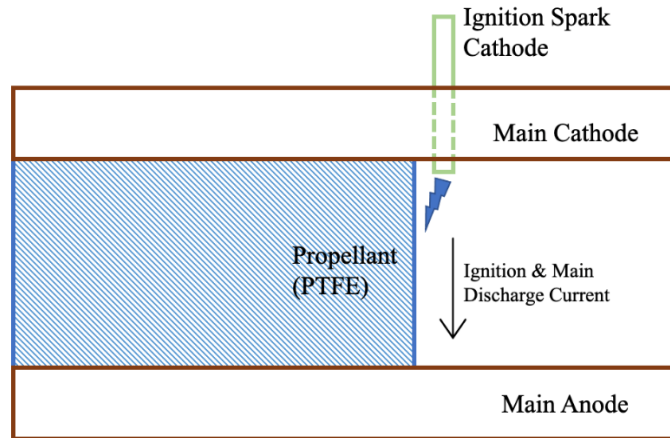


Figure 3.22 - PPT ignition spark diagram representation

While extremely vital to the operation of a PPT, the ignition spark circuit will not be reproduced for the performance analysis. This is due to that fact that the analysis will primarily be of the RHS and LHS current loops shown previously in Fig. 3.16.

3.5 Electrode & Propellant Characteristics and Parametric Analysis

The electrode and propellant geometry, the entire basis of this reports analysis, will be discussed in this section. This component is the last that will receive a parametric analysis since analyzing the effects of the electrode geometry on PPT performance requires the input of the parameters from most of the other components and systems. What is clear in most of the research done for this report, is that electrode geometry plays a fundamental role in contributing to overall PPT performance.

3.5.1 Electrode Characteristics and Necessary Background

Before an analysis can be performed, a discussion around the classifications of PPT electrode geometries must be discussed. As it stands today, there are two major electrode geometry classifications. The first is the coaxial configuration, previously mentioned in the first chapter of this report, where a cylindrical anode is surround concentrically by cathode of larger radius. The second and most pertinent electrode configuration is the “Rail” configuration. Within this configuration there are multiple modification that can be made. [30] They are listed below as follows: [30]

- Electrode Configuration: Rail
 - Modification: Shape
 - Rectangular
 - Tongue

- Modification: Angle, φ
 - Parallel ($\varphi = 0$)
 - Flared ($\varphi > 0$)

The parallel-rectangular-rail configuration is the one that will be considered for this reports PPT design. One thing is clear, even though they were not considered for this design, PPT electrodes that incorporate tongue and flared angle configuration see signification increases in performance. This is found to be true in research performed by W.H. Guman and P.J. Palumbo on electrode geometry in PPT. Their work finds that for breech-fed PPTs, increasing φ to 20° leads to a 3.4% increase in T_{sp} , a 9.1% increase in I_{sp} , and a 6.1% increase in η . This is the same research that found that increasing the aspect ratio h/w by increasing the electrode gap, led to an increase in I_{sp} . The value of η also increases but will eventually reach a maximum after which it will begin to decrease. Meanwhile, T_{sp} is the only term that immediately decreases. When this test was also done for a decreasing h/w by increasing w , it was determined that I_{sp} , T_{sp} , and η all decrease while the mass ablated per pulse in increases. As a result, it was concluded that increasing h/w by increasing h led to the most favorable performance enhancements in PPTs. The next section features an analysis of this trend, showing how it affects performance. [7]

3.5.2 Electrode Parametric Analysis

Based on previous research, it can be assumed that – excluding E' – the critical design criteria for maximizing the performance of a PPT is the aspect ratio h/w . In past research, estimating the effect of this parameter's value on overall performance was determined using the equation shown below, Eq. 3.18. In this equation, α and β are both constants that are numerically determined, and A_p refers to the exposed surface area of the propellant. While the relationship between discharge energy and propellant surface area is valuable for estimating performance, it is inadequate at correlating the effects of various values of h , w , and φ on performance. As a result, modern derivations of the relationship between electrode geometry and performance, like the MEMTA model presented in chapter 2, tend to rely on how electrode geometry modifies the inductance gradient L' . [36]

$$I_{sp} = \alpha \left(\frac{E'}{A_p} \right)^\beta \quad (3.18)$$

The inductance gradient, or total inductance per unit length, while not explicitly mentioned in the MEMTA model, forms the basis for how the MEMTA model relates electrode geometry and performance. For a PPT, L' represents the total circuit inductance derived along the distance of the electrode length. This means it's characteristic behavior can be estimated using the dimensions of the chamber it's traveling in. This can be seen in Eq. 3.19, shown below, where the inductance per unit length along the acceleration axis is purely defined by the electrode geometry. The resulting unit is $\mu H/m$.

$$L' = 0.4 \left[\ln \left(\frac{2h}{w+d} \right) + \frac{3}{2} - \frac{h^2}{4l^2} \right] \quad (3.19)$$

This equation assumes that the electrode configuration is able to satisfy $h > w \approx d$, which is true for the electrode geometries that are analyzed in this report. This term – the inductance gradient – plays a fundamental role in the determination of the electro-mechanical component of the impulse bit. Eq. 3.20, shown below, is the simplified form of the impulse bit, which can be solved and rearranged to produce the expression for the electromechanical component of the impulse bit shown on the left-hand side of the integral in Eq. 2.45. [36]

$$I_{bit} = \frac{L'}{2} \int_0^{t'} [I(t)]^2 dt \quad (3.20)$$

Pursuing a greater performance gain in a PPT means increasing the coupling between L' and I_{bit} , which means that an optimization of possible electrode configurations must be performed. In research performed by S.J. Pottinger, the maximum value of h and w for a μ PPT was set at 15 mm and 10 mm, respectively. In keeping with the existing experiment heritage for μ PPTs available, this parametric analysis will follow the same classification. Within the same set of research, the inductance showed a partially linear correlation positive between L' and h at a constant w , d and l . The correlation is only partial due to the small range of h and w values considered. This report seeks to investigate this same parameter but at a wider range of values. It is likely that the correlation would not remain linear. The partial correlation can be seen in Fig. 3. [36]

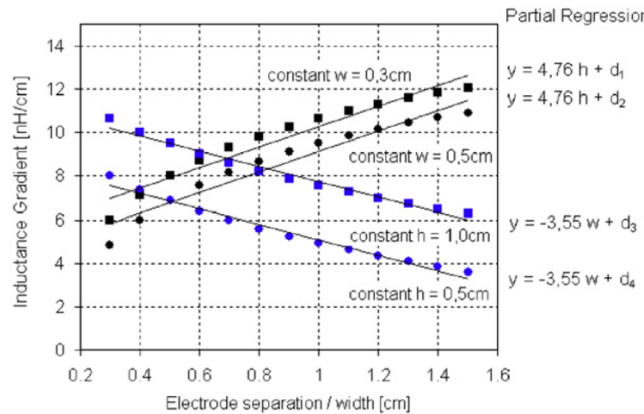


Figure 3.23 - Inductance gradient as a function of electrode separation or width

Using Eq. 3.8, it's possible to set a preliminary range of values for the electrode geometry. For standard PPTs it is common for the electrode length to satisfy $l \gg h$. Due to this, the value of l will set to a value that is four times the length of the gap when $w = h$, since w will be fixed for this analysis. [36] Along with this, based on the limits of “micro” classified PPTs, this electrode geometry analysis will look at a range of electrode gap values at three different static electrode widths. These four will be:

- $w_1 = 3 \text{ mm}, (l_1 = 12 \text{ mm})$

- $w_2 = 5 \text{ mm}, (l_2 = 20 \text{ mm})$
- $w_3 = 7 \text{ mm}, (l_3 = 28 \text{ mm})$
- $w_4 = 10 \text{ mm}, (l_4 = 40 \text{ mm})$

Since this report calls for an analysis of aspect ratio values between 1 and 4, the values needed for h will be set for each w such that h/w satisfies the required range. For the previously chosen values of w this means four ranges of h that satisfy $1 \leq h/w \leq 4$:

- $3 \text{ mm} \leq h_1 \leq 12 \text{ mm}$
- $5 \text{ mm} \leq h_2 \leq 20 \text{ mm}$
- $7 \text{ mm} \leq h_3 \leq 28 \text{ mm}$
- $10 \text{ mm} \leq h_4 \leq 40 \text{ mm}$

The plot of the inductance gradient is shown below in Fig. 3.24, where the vertical line set at 15 cm is the maximum electrode gap limit for a micro-class PPT. Here, as well, the unit for L' was changed to nH/cm so that whole numbers could be used on each axis.

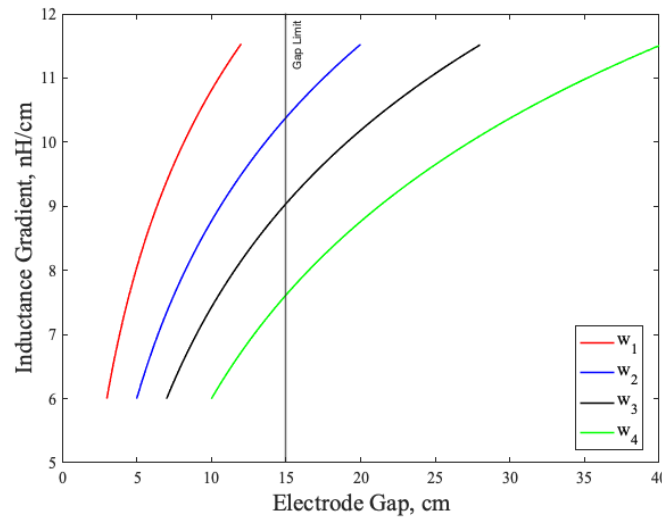


Figure 3.24 - Inductance gradient for a range of electrode gaps at four electrode widths

Of the four considered electrode widths, just three are able to reach the gap limit within their 1 to 4 h/w value sweep. That said, each one of these three surpasses the gap limit proposed by previous research [36]. This is actually acceptable since the scope of this reports analysis includes analyzing h/w values above and below conventional limits. As a result, the most optimized w value is that of w_2 . This means that the design electrode parameters for this report are as follows:

- Electrode width, w : 5 mm
- Electrode thickness, d : 5 mm
- Electrode length, l : 20 mm
- Electrode gap, h : 5 – 20 mm
- Electrode aspect ratio, AR : 1 – 4

These values are also in agreement with electrode geometry data taken from the heritage PPTs being considered for this trade analysis, shown below in Table 3.4. Furthermore, based off of this

data, it would be appropriate to assume that idea performance might possibly be seen when $AR = 2$. This is solely based on the fact that this value is the most commonly found in the PPT and μ PPT listed in the table.

Table 3.4 - Electrode design and performance qualities of eligible PPT and μ PPT

PPT Name	Material	AR (h/w)	Shape	Flare
TMIT-PPT [15]	Molybdenum	2	Rect.	0
Breech-fed PPTCUP [24]	Tungsten Copper	2	Rect.	0
Side-fed PPTCUP [25]	Tungsten Copper	2	Tongue	20
Busek BmP-220 [27]	--	--	--	--
Dawgstar μ PPT [29]	--	4	Rect.	0
LES-6 [31]	--	--	--	--
CubeSat μ PPT [13]	Tungsten Copper	2	Rect.	20
AV3 Dual-Axis PPT [33]	--	1.5	Tongue	20

Based on research performed by W.J. Guman on the effects of electrode geometry on PPT performance, it was determined that the correlation between I_{sp} and the area of the exposed propellant A_p can be expressed with an exponential function. In the case of a breech-fed parallel electrode PPT, the value of A_p is entirely dependent on the values of h and w . More specifically, the surface area of the exposed propellant is the product of these two terms, as seen in Eq. 3.21, below. The exponential function that correlates A_p and I_{sp} , Eq. 3.22 below, is based on approximations performed by Guman. The equation is valid for all different propellant-feeding geometries at low power levels ($< 5J$). [32]

$$A_p = hw \quad (3.21)$$

$$I_{sp} = 317 \left(\frac{E'}{A_p} \right)^{0.585} \quad (3.22)$$

Using Eq. 3.13 and the chosen ranges for I_{sp} and h , it is possible to choose an input discharge energy. Solving for I_{sp} at whole number discharge energies between 2 and 6 produces the plot below, Fig. 3.25, where the energy density is the discharge energy divided by the exposed propellant area (E'/A_p):

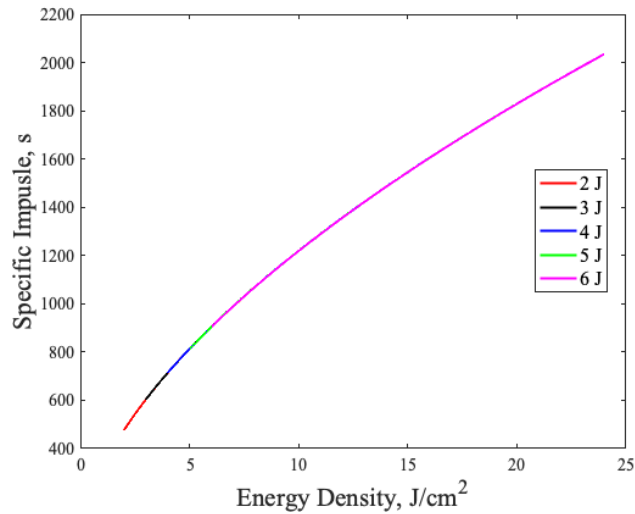


Figure 3.25 - Specific impulse and energy density correlation plot for five discharge energies

Each of the colored sections in this plot, representing the curve created by Eq. 3.22, shows the range of I_{sp} values possible for each discharge energy that are not already values for the proceeding discharge energy value. Zooming into the I_{sp} range being considered for this design produces Fig. 3.26 shown below:

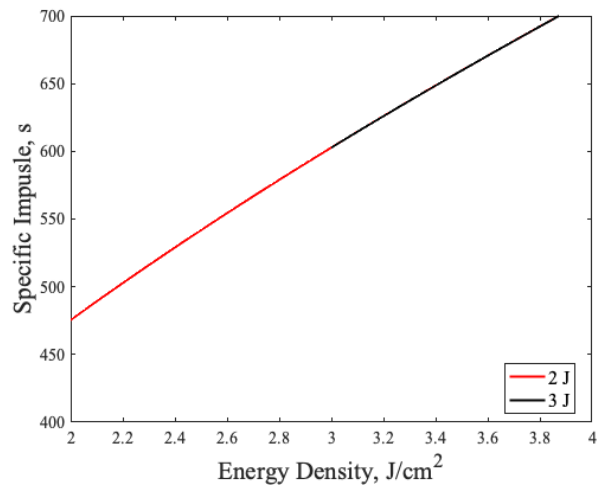


Figure 3.26 - Specific impulse and energy density correlation plot for specified impulse range

In this plot, only the lower bounds of the 2 Joule and 3 Joule curves are visible. Which means that, for a low energy μ PPT, it would be appropriate to be designed to operate at 2-3 J. For the sake of optimizing performance, for this design, a range of 2 to 3 Joules will be chosen as the design discharge energy.

4 Full System Design Parameters

To best model a realistic system for this analysis, each component must be selected based off of real-life analogs. As a result, this system will take on the same inefficiencies that are involved in the operation of a testable PPT. This means that the design of each component of the PPT system must be bound by the functional constraints of the real-life components chosen to perform their operation. Along with this, the entire system must also adopt constraints that enable it to satisfy the structural and operational requirements commonly placed on CubeSats. Based on heritage PPT designs, it is possible to extrapolate constraints that appropriately satisfy μ PPT requirements for CubeSats. These will guide the parameter selection process and define the boundaries of a realistic μ PPT design.

4.1 Overall System Performance Constraints

One of the most fundamental constraints that bounds the design of the overall PPT system is the CubeSat form factor. This means that the circuit for the PPT must fit on a PCB (or two) of overall dimensions 9×9 cm, length by width [3]. Along with this, HV electronic components tend to be larger and require a significant amount of space in between pins to prevent internal arcing, so the system must be no more than 0.5U (5 cm) in height. Since this would take up far too much room in a 1U CubeSat, this design will be considered for a 3U CubeSat [3]. This lies within the same specifications as the CubeSat μ PPT considered for the trade analysis in chapter 3, so similar assumptions were made for this μ PPT. [13]

For a 3U CubeSat mission spanning 3 years at an orbital altitude of 600 km, the total required orbital maintenance impulse would be roughly 30 Ns [13]. According to performance studies done by Guman, the total required propellant mass for a mission can be determined by dividing the total impulse by the specific impulse as can be seen below in Eq. 4.1 [32]. Along with this, the total mass of the system must not surpass 350 g. This factors in structural weight and wire harnesses [3].

$$m_p = \frac{I_{tot}}{gI_{sp}} \quad (4.1)$$

Solving for Eq. 4.1 using a total impulse of 30 Ns and the specific impulse range determined in the previous chapter (400 – 700 s), the total required propellant mass needed for the mission must be a minimum of 4.4 g and a maximum of 7.7 g. Since these values of m_p represent a minimum at each of the I_{sp} values, the chosen values must be increased. As such, the chosen values will now become 5 g and 8 g to allow for a 5% error margin. From these design considerations and those discussed in chapter 3, a table of all of the available design parameters can be produced. This is shown below in Table 4.1:

Table 4.1 - Pre-constraint design parameters

Design Parameter	Value	Design Parameter	Value	Design Parameter	Value
I_{tot}	30 <i>Ns</i>	E' range	2 – 3 <i>J</i>	w	5 <i>mm</i>
M_{max}	350 <i>g</i>	V_0 (design)	1500 <i>V</i>	d	5 <i>mm</i>
m_p range	5 – 8 <i>g</i>	C range	1.8 – 2.7 μF	h range	5 – 20 <i>mm</i>
I_{sp} range	400 – 700 <i>s</i>	l	20 <i>mm</i>	AR	1 – 4

The remaining design parameters left to be determined are the capacitance C , discharge energy E' (chosen from the capacitance), total system resistance R_T , and total system inductance L_T . These parameters are primarily governed by the properties of the capacitor and the PPU. In the upcoming sections, design constraints will be derived and utilized to determine the appropriate design parameters for the capacitor and PPU.

4.2 Capacitor Design Constraints and Parameter Selection

Due to the simplicity of the capacitors needed for a μPPT , there are only two parameters that constraint its design. These two are the total mass and the contribution to the critical damping condition previously discussed in section 3.4.1. For this design, Film capacitors and ceramic capacitors are being considered. Ultimately, the final design will only include one of these two options, so it is imperative that the constraints determined in section assist with type selection.

Simply put, for this μPPT design there are two mass-dependent configurations possible: capacitor bank or single capacitor. At the low capacitances being considered for this design, a small bank of HV ceramic capacitors or a single HV film capacitor are acceptable for operation. This is due the capacitance limitations placed on capacitors of both types when operating at voltages greater than 1000 V. This means that deciding between the two relies solely on the amount of mass they introduce to the full system. As such it would be appropriate to select actual capacitors that can be purchased for use. Table 4.2, below, shows all of the capacitors being considered for this and their relevant properties [38]:

Table 4.2 - Real-world properties of relevant capacitors [38]

Type	Model	Capacitance (μF)	V-Rating (<i>kV</i>)	Resistance (<i>m</i> Ω)	Inductance (<i>nH</i>)	Mass (<i>g</i>)
Ceramic	KEMET X7R	0.16	1.5	16	120	0.79
Film	KEMET R75H	0.82	1.6	3.9	20	15
Film	KEMET R75H	1.20	1.6	4.0	20	15

As was mentioned in the previous chapter, film capacitors, while capable of higher capacitances at high voltage ratings, can be tens of times heavier by mass than ceramic capacitors. In this case, the film capacitors being considered are almost 19 times heavier individually. In fact, a quick analysis of the mass of these capacitors shows that to attain the upper bound of the capacitance range being considered, 2.7 μF , 17 KEMET X7R ceramic capacitors are needed. At this number the total mass of the capacitor bank would be 13.43 *g*, which is 10.5% smaller than

the mass of both film capacitors being considered. Ultimately, this capacitor is the most appropriate for this μ PPT design.

4.3 Power Processing Unit Design Constraints and Parameter Selection

Along with the capacitor bank, the power processing unit is constrained by its mass and critical damping condition. While determining an appropriate mass is simple since the total system mass has already been determined, the damping ratio that can be derived from the critical damping condition requires some background. Specifically, while it would be ideal to have a critically damped current and voltage oscillation, it is not a realistic solution for a PPT. Fig. 4.1 and Fig. 4.2, shown the current curves for the discharge of heritage μ PPT experiments at a similar discharge energy level as the one being considered for this report. [13][36]

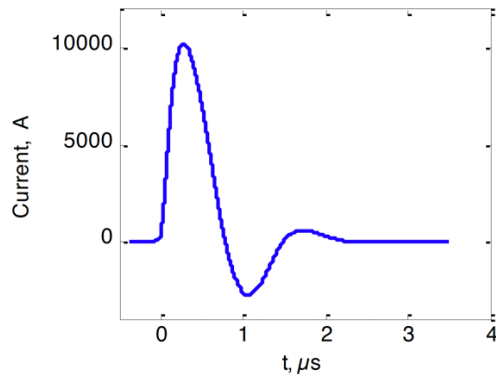


Figure 4.1 - Current plot of Coletti μ PPT [13]

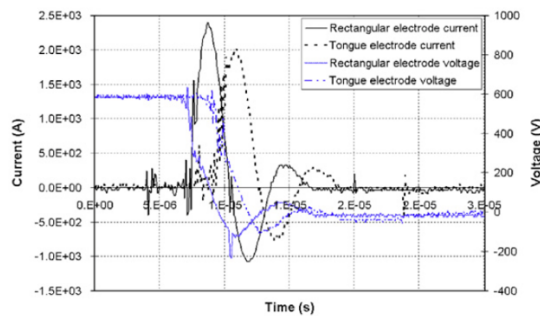


Figure 4.2 - Current plot of Pottinger μ PPT [36]

In both of these plots, curve dampen after just two peaks. This indicates that, while still underdamped, these plots undergo much dampening. In an ideal case, according to research performed by Coletti, the resistance and inductance should be around 0.07Ω and $20 nH$. This results in a damping ratio of 0.196 for their design [13]. In light of the similarities between this μ PPT and the one in this design, this value for the damping ratio was chosen as the benchmark to achieve for finalizing the design.

With the damping ratio in consideration, it's now appropriate to present the real-life components needed to achieve the performance standards presented in the previous sections for

the PPU. From there, the characteristic parameters of these components will be assessed to determine their influence on the operation of the μ PPT. Below, in Table 4.3, is a list of all of these components including all of their relevant properties. Any section left blank in the table below represents a value that is not needed to analyze the performance of this μ PPT, since the current pulse occurs only within the RHS loop of the circuit, as seen in Fig. 3.16. The electrode and propellant masses were also determined, though they are not components of the PPU, since their masses has yet to be discussed.

Table 4.3 - Relevant PPU component properties

Component	Model	Mass (g)	Inductance (nH)	Resistance (m Ω)
DC-DC Converters	EMCO FS20-12	45	--	--
	EMCO E60	85	--	--
Switches (2x)	Sensata-Cynergy3	62	5	60
Controller	ItsyBitsy MO	2.7	--	--
Ignition Capacitors	KEMET	2.3	--	--
PCB and Wiring	OshPark	40	2	TBD
Electrodes*	--	90	TBD	TBD
PTFE	--	6	--	--

Taking the total mass of these components along with the capacitor and electrodes results in a total system mass of 347 g was determined. This value sits just below the previously determined maximum of 350 g but is acceptable since the maximum was determined in light of the mass of the structure around the full μ PPT system. Along with total mass, the total resistance and inductance need to be determined. Fortunately, the only resistances that are left to be determined are that of the electrodes and leftover required resistance satisfied by the PCB wiring and in-series resistors. Eq. 4.2 below shows the resistance of a copper electrode, where ϵ_e is the electrical resistivity of copper and l_f is the total length including past the propellant. [34] (Equations below for inductance [39])

$$R_{pe} = \frac{2\epsilon_e l_f}{wd} \quad (4.2)$$

Solving for the R_{pe} in Eq. 4.2 above results in a total electrode resistance of 26.8 $\mu\Omega$. This value is extremely small, but it is to be expected since copper is a very strong conductor. From this term and the other resistance terms, including the plasma resistance, and the total inductance it is possible to determine how much more resistance is needed to satisfy $\zeta = 0.196$. To do this, the inductance of the electrodes and plasma must first be determined. Fortunately, the electrode and plasma inductances are functions of the electrode geometry.

In Eq. 4.3, shown below, the self-inductance of each individual electrode is determined using a standard approximation of the self-inductance of a conductor with a rectangular cross-section. In this equation, the term K_L is a coefficient based on the electrode properties which, in this case is equal to 0.00177. [39]

$$L_{el} = 0.002l \left[\ln \left(\frac{2l}{w+d} \right) - K_L + 0.5 \right] \quad (4.3)$$

The mutual inductance of the electrode is also needed to determine the total inductance of the circuit. Mutual inductance refers to the electromotive force of one volt resulting from a current passing through multiple interacting mediums. This principle operates only in circuits that experience a current flux. Eq. 4.4, below, shows the mutual inductance determined using standard approximation of two parallel conductors with a rectangular cross-section. This equation is only valid when $w = d$, $w \leq l$, and $d/h < 1$ are all satisfied, which in the case of this μ PPT is true. Furthermore, the term K_M is equal to 0 in the case of this specific electrode cross-section geometry. [39]

$$M_{el} = 0.002l \left[\ln \left(\frac{2l}{h} \right) + \frac{h}{l} - \frac{h^2}{4l^2} - K_M - 1 \right] \quad (4.4)$$

Lastly, the self-inductance of the plasma is also needed to complete the inductance calculation. In this case, the plasma inductance at any time during the pulse can be approximated as straight conductor with the same cross-sectional properties as the electrode. This time, the “length” of the conducting “wire” is equal to the gap between the electrodes. The value for K_L remains the same as well. Eq. 4.5, below, shows this function that results in solving for L_p that was presented in Chapter 2. [39]

$$L_p = 0.002h \left[\ln \left(\frac{2h}{w+d} \right) - K_L + 0.5 \right] \quad (4.5)$$

The sum of these terms becomes the plate electrode inductance, or L_{pe} , that was first introduced in Chapter 2. It should also be noted that, for Eq. 4.3, 4.4 and 4.5, the values of l , w and d are measured in cm and the resulting units is μH . These values were converted to nH before being input into the total electrode inductance equation. Eq. 4.6 below shows this sum, where M_{el} is subtracted due to its opposing effect on the total inductance in material.

$$L_{pe} = 2L_{el} - M_{el} \quad (4.6)$$

Ultimately, solving for the total inductance L_T , requires the use of Eq. 2.36. In this equation, the lead, wire and other electronic component inductance L_e , is approximated to equal $7 nH$. This is because the total wire density is similar to that of the copper electrodes which also has around $7 nH$ of inductance. This results in the total circuit inductance of $35 nH$ at $h = 20 mm$ and $24.3 nH$ at $h = 5 mm$.

Taking the total circuit inductance and capacitance it's now possible to determine the total required resistance by solving for R_T in Eq. 4.7, below, which is based on critical damping condition equation [13]. In this equation, the term ζ_{req} refers to the required damping ratio needed

to for a well-damped solution. Since it is likely that this system will experience higher performance at greater values of h , the values for L_T were determined for when $h = 20 \text{ mm}$.

$$R_{Treq} = \sqrt{\frac{4\zeta_{req}L_T}{C_T}} \quad (4.7)$$

Using Eq. 4.7, a final resistance of $101 \text{ m}\Omega$ was determined. Subtracting out the plasma, electrode, capacitor, and switch resistances leads to a value of $36 \text{ m}\Omega$ needed to be satisfied by the rest of the components and an in-series resistor.

4.4 Full System Parameters

After solving for all the component properties in this μPPT , the resulting full system parameters are as follows, listed below in Table 4.4:

Table 4.4 - Full μPPT system design parameters

Design Parameter	Value	Design Parameter	Value	Design Parameter	Value
I_{tot}	30 s	h	$5 - 20 \text{ mm}$	L_c	7.06 nH
M_{sys}	347 g	w	5 mm	R_c	$0.941 \text{ m}\Omega$
m_p	6 g	d	5 mm	L_p	7.54 nH
E'	3 J	l	20 mm	R_p	$3.3 \text{ m}\Omega$
V_0	1500 V	AR	$1 - 4$	L_{pe}	20.8 nH
C	$2.7 \mu\text{F}$	T_e	18000 K	R_{pe}	$0.0268 \text{ m}\Omega$
n_c	17	n_e	2.534×10^{22}	L_e	7 nH
t'	$4 \mu\text{s}$	m_{bit}	$4 \mu\text{g}$	R_e	$96 \text{ m}\Omega$

4.5 Mass Bit and Gas-dynamic Impulse Approximation

Before a performance analysis methodology can be discussed, there are two approximations that must be address so that their resulting values have reliable justifications. The first of these two is the approximation of the mass ablated per pulse or mass bit m_{bit} . Due to the complex nature of the approximation produced in chapter 2, for the ablation process and for the sake of expediency, the value of m_{bit} was approximated using the regression plot of m_{bit} based on historic data. Using Eq. 3.3 and solving for the m_{bit} at 3 J , a resulting value of $4 \mu\text{g}$ was determined.

The second approximation utilized for this performance analysis is that of the plasma properties, particularly, the electron temperature T_e and electron number density n_e . These two

terms appear in the gas-dynamic component of the impulse bit seen in Eq. 2.45. and in the formulation for the plasma resistance seen in Eq. 2.37.

Researchers at Fudan University, performed a spectral analysis on the plasma plume of a 5 J PPT. From this process, it is possible to extrapolate the profiles of the spectral lines emitted from the plasma plume. These spectral lines are subject to various broadening and shifting mechanisms, but in this case the most important broadening effect analyzed was Stark broadening. Doing this results in a set of functions that allowed the researchers to define the properties of the plasma plume. [40]

Ultimately, that analysis resulted in experimentally determined values for n_e and T_e of a 5 J PPT's plasma plume. These values are $n_e = 2.534 \times 10^{22} m^{-3}$ and $T_e = 18000 K$. It is also important to note that while this analysis was performed on a 5 J thruster, it was determined that for a range of low discharge energies ($E' < 10$), the changes to n_e and T_e are minimal and in some cases negligible. As such, these values were adopted for this designs 3 J PPT. [40]

5 Thruster Performance Analysis and Results

In this chapter, the full system performance analysis is performed for the thruster designed for this report. As previously mentioned, the electrode and propellant aspect ratio AR , will be varied from 1 to 4 to investigate how this variance affects the overall performance. Along with this, the analytical result that this design produces will be measured against a tested system with similar system properties to assess how this configuration varies from a heritage design. The tested system being considered is a 2-3 J μ PPT with an identical electrode width, developed and tested by S.J. Pottinger. Ultimately, much like a control system response, the response of the circuit during each pulse is dependent on the gain value of the resistance, inductance, and capacitance. This reports design and the Pottinger μ PPT will utilize different values for these three terms, so this analysis will also reveal the improvements and losses made as a result of the parameter choices made for this design.

5.1 MATLAB Implementation

After setting the up the input variables, the system must be represented analytically and integrated to produce a result for the performance variables. To do this, MATLAB was utilized to manage the component variables and apply the integral approximates needed to find the integral of Eq. 3.13. This process is relatively simple. This can be seen in the performance analysis portion of the code, shown in the Appendix. It shows that for some variables, its representative order of magnitude must be taken into consideration.

One part of this code that must be noted is that the integral for this analysis requires an “ArrayValued” condition within it so that h can be varied on its own array while the entire function varies with time in the integral. This is fundamental so that MATLAB integrates the entire current function at each value of h .

5.2 System Performance

As was mentioned at the beginning of this chapter, the performance trends for a μ PPT of varying aspect ratio will be done in this section. To determine the performance values relevance to heritage data, the performance data from the μ PPT developed by S.J. Pottinger and associates (Pottinger’s μ PPT) was extrapolated and compared to this data from design. This μ PPT was chosen due to its almost identical electrode configuration and similar energy level. Table 5.1, below, shows the design parameters for Pottinger’s μ PPT, using the subscript “ pp ” to refer to “Pottinger’s PPT”.

Table 5.1 - Pottinger μ PPT design parameters [36]

Design Parameter	Value
C_{pp}	$6.0 \mu F$
E'	$2 J$
m_{bit}	$3 \mu g$
h_{pp}	$5 - 15 mm$
w_{pp}	$5 mm$
d_{pp}	$3 mm$
l_{pp}	$15 mm$

5.2.1 Current and Voltage Transients

As was shown in chapter 4, the current and voltage transient responses are functionally dependent on the geometry of the electrodes. As a result, any discrepancy found between the transients for this design's and Pottinger's μ PPT is completely reliant on the values of R_T , L_T and C determined for both designs. In Figure 5.1, below, the current transient response to the pulse when $h = w = 5 mm$, is shown. In this plot, the total pulse time comes out to around $3 \mu s$ with the current peaking at around $8.5 kA$. This plot bears similarity with the plot of the current transient produced by Coletti, shown in Fig. 4.1, which is likely due to both being low inductance and high resistance circuits.

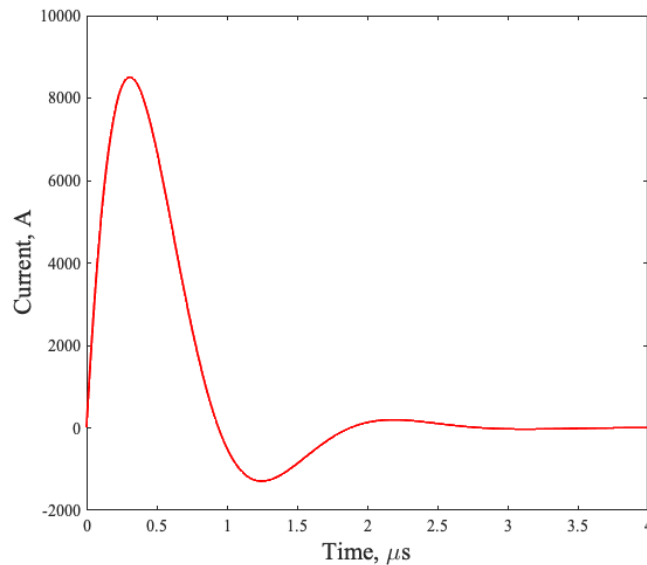


Figure 5.1 - Current transient response when $AR = 1$

When electrode gap is increased to $20 mm$ from $5 mm$, the current produces a different transient response. This can be seen below in Fig. 5.2. In this plot, the current transient peaks at $7.9 kA$ while the pulse time t' is around $4 \mu s$. Overall, increasing the aspect ratio results in a lower peak current but increase the overall pulse time.

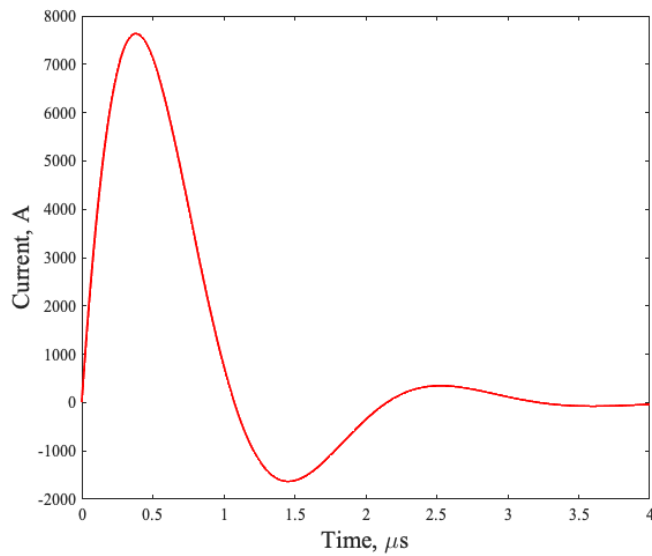


Figure 5.2 - Current transient response when AR = 4

When comparing these results with the current transient for Pottinger’s μ PPT it’s clear to see just how much variance in the values of inductance, resistance and capacitance influences a PPTs pulse response. Fig. 5.3, shown below, portrays the current transient of Pottinger’s μ PPT laid on top of the current transient for this designs μ PPT. The resulting oscillation for Pottinger’s μ PPT is a result of the high inductance ($> 100 \text{ nH}$) and relatively higher capacitance used for its design parameters. It is also important to note that the current transient curve is a representative plot, meaning it shows the function as it exists numerically. Realistically, due to the nature of the spark pulse, the current would taper off to zero after the second peak. In this case, when the current hits zero at $9 \mu\text{s}$, the current will remain zero. Ultimately, the longer pulse time of $9 \mu\text{s}$ and lower current peak of 3.8 kA are the result of Pottinger’s inductance derivation process, which varies from the one utilized for this project. [36]

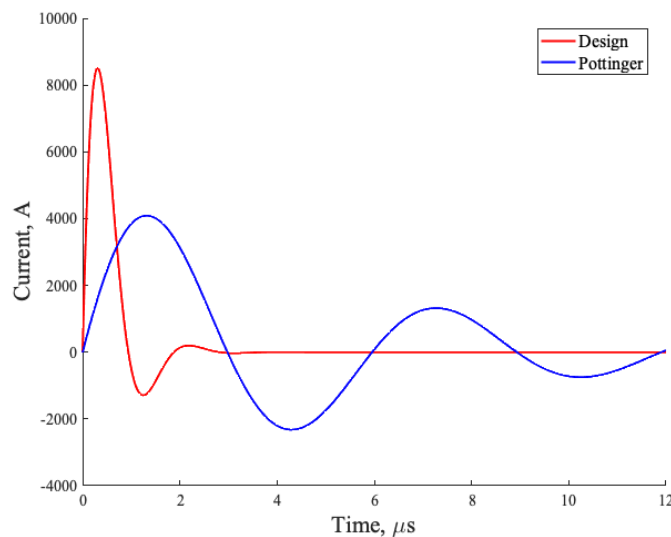


Figure 5.3 - Current transient when AR = 1 of the designed μ PPT and Pottinger's μ PPT

When the aspect ratio is increased to 3, Pottinger's μ PPT responds in the same manner as this μ PPT design, with the current peak decreasing to 3.3 kA and the pulse time increasing to 9.6 μ s. This can be seen below in Fig. 5.4:

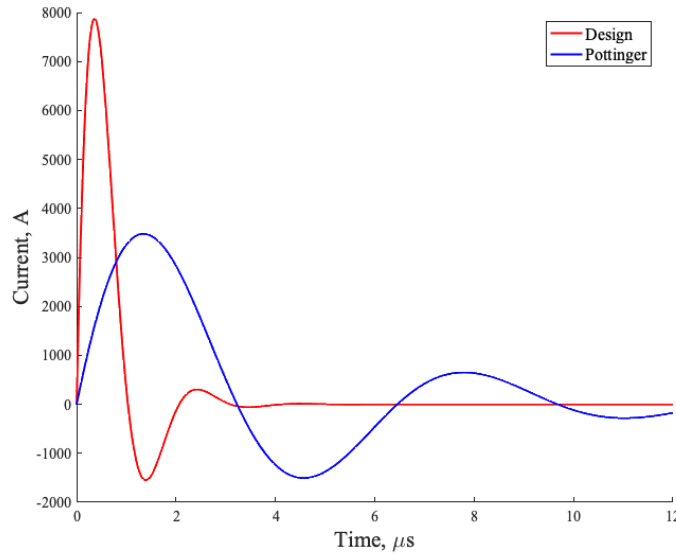


Figure 5.4 - Current transient when AR = 3 of the designed μ PPT and Pottinger's μ PPT

This variance in system response can also be seen in the voltage transient for the pulse. Fig. 5.5 and 5.6 below, shows that the low inductance values and 1500 V discharge voltage results in a shorter voltage pulse and quick dampening, which is also seen with the current. At a higher aspect ratio, the pulse time increases for both μ PPTs. In the case of Pottinger's μ PPT, the discharge voltage is 816 V.

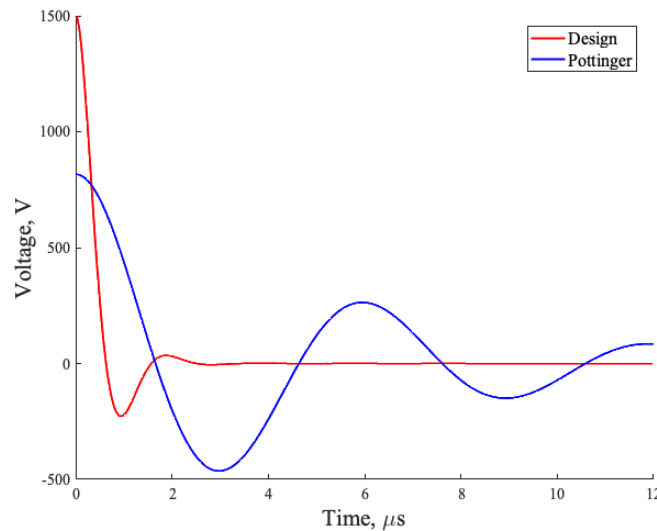


Figure 5.5 - Voltage transient when the AR = 1 of the designed μ PPT and Pottinger's μ PPT

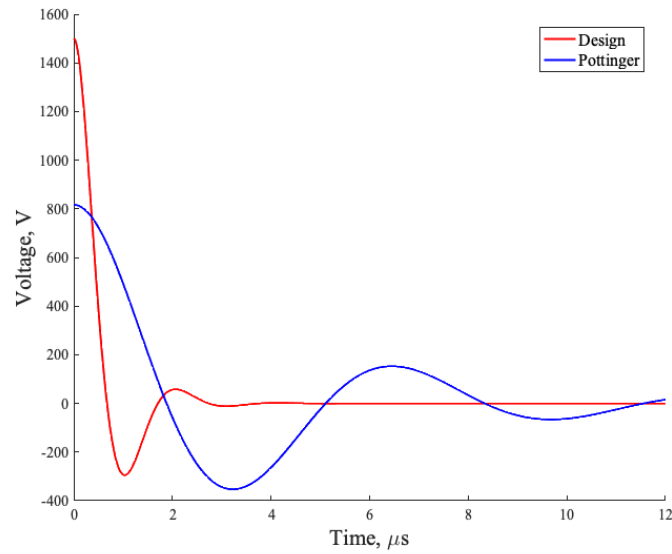


Figure 5.6 - Voltage transient when AR = 3 of the designed μ PPT and Pottinger's μ PPT

5.2.2 Performance Characteristics

Ultimately, these current transients play a significant role in the performance characteristics of a μ PPT. Since the current is heavily dependent on the inductance, capacitance, and resistance, it follows that the impulse bit, a function of the current, is also dependent on these values. The values of these parameters are numerically dependent on the geometry, so for the sake of performing a comparative analysis, each performance parameter will be evaluated as a function of the aspect ratio. In this case, the aspect ratio is being varied from 1 – 4 mm with a fixed w of 5 mm and with the AR increasing with increasing h .

Fig. 5.7, shown below, is a plot of the damping ratio ζ as a function of the aspect ratio. In this plot, the designed μ PPT achieves aspect ratios greater than that of Pottinger's. This is due to the fact that Pottinger determined high inductance values for the μ PPT's electrode-plasma interaction. In Pottinger's case, increasing the aspect ratio led to a decreasing inductance. This results in an increasing ζ value, which can be seen in the figure. Inversely, this design has a higher average ζ due to its lower inductance and has an increasing inductance with increasing aspect ratio, which causes decreases in ζ until it reaches the required value, ζ_{req} , at $AR = 4$. This is important, as this aspect has an effect on the trends on the performance with increasing aspect ratio. Mainly that, with the higher inductances, the performance values should increase and should do so more rapidly than with Pottinger's μ PPT. [36]

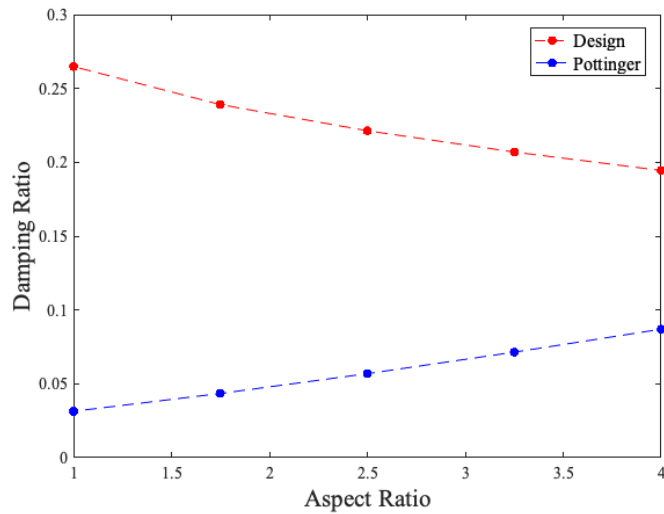


Figure 5.7 - Damping Ratio as a function of the aspect ratio for the designed μ PPT and Pottinger's μ PPT

The first plot that shows that assumption to be true is the plot of the impulse bit I_{bit} and the aspect ratio. In this plot, the I_{bit} for the designed μ PPT starts lower than Pottinger's μ PPT at a value of $5.6 \mu\text{Ns}$. Eventually, with increasing AR and due to a higher slope, the I_{bit} of the designed μ PPT quickly surpasses the I_{bit} of Pottinger's μ PPT, finally reaching a value of $15.8 \mu\text{Ns}$ at $AR = 4$. These values are considerably low for many other μ PPT but at this configuration these values are expected. [36]

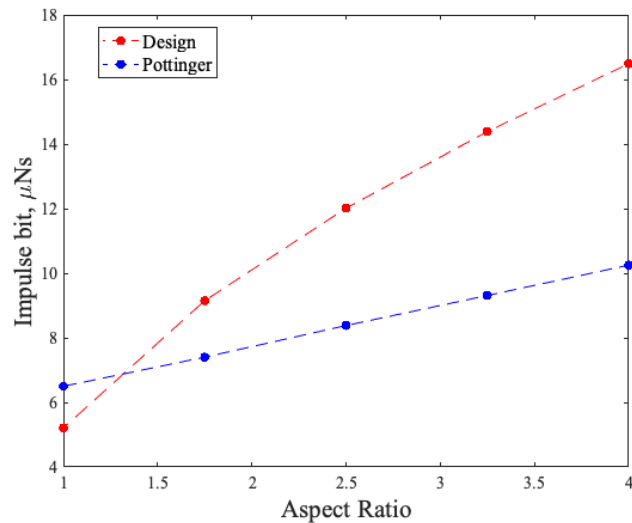


Figure 5.8 - Impulse bit as a function of the aspect ratio for the designed μ PPT and Pottinger's μ PPT

For the performance of the specific impulse I_{sp} , Fig. 5.9, below, shows a similar trend. The I_{sp} of the design starts well below Pottinger's μ PPT at a value of 132 s at $AR = 1$. This value is extremely low for any μ PPT but as AR increases so does the I_{sp} until it reaches 420 s at $AR = 4$. This value is acceptable and even agrees with the design range determined for this μ PPT. [36]

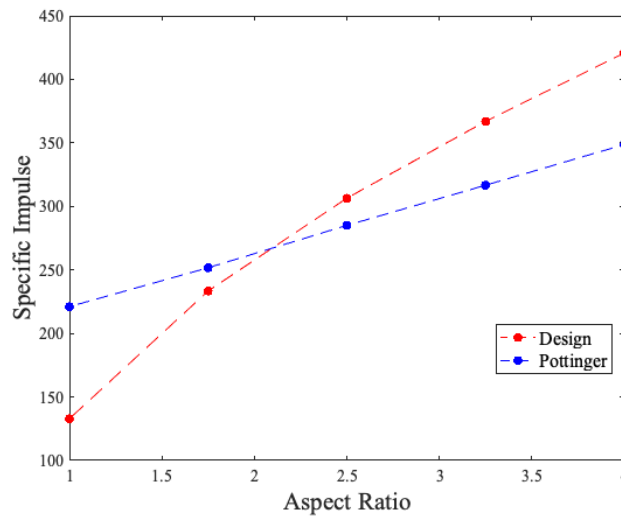


Figure 5.9 - Specific impulse as a function of the aspect ratio for the designed μ PPT and Pottinger's μ PPT

Lastly, the resulting propulsive efficiency range produced from this analysis shows efficiency values well below those seen in flight heritage μ PPTs. While this is not ideal, it is to be expected since this configuration represents the simplest and least optimized configuration for the electrodes. Fig. 5.10, below, shows that the efficiency range of Pottinger's μ PPT also agrees with the one designed for this report. Like with the other performance values, the propulsive efficiency starts low below the value for Pottinger's and eventually increases to be higher than it. At its lowest, when $AR = 1$, $\eta = 0.1\%$ and at its highest, when $AR = 4$, $\eta = 1.1\%$, increasing by a whole order of magnitude.

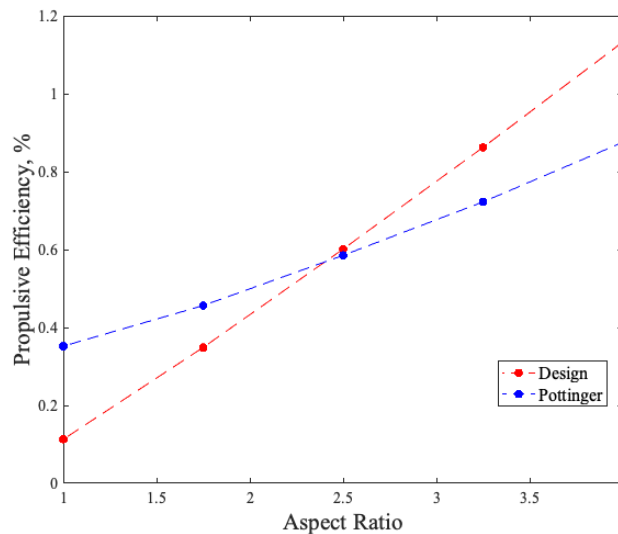


Figure 5.10 - Propulsive efficiency as a function of the aspect ratio for the designed μ PPT and Pottinger's μ PPT

The performance data presented above shows that most assumptions about the performance of a PPT with varying AR are correct. The most important of these assumptions is that increasing AR by increasing h is the ideal method for optimizing performance. In fact, increasing AR by

decreasing w will lead to lower performance as AR increases. To visualize this, Fig. 5.11, 12 and 13, shown below, portrays an increasing AR , where $h = 2 \text{ mm}$ and $w = 0.2 - 0.5 \text{ mm}$. When the value of AR increases with decreasing w , each performance parameter increases marginally until the AR value corresponding to $w = 0.3$, after which the values begin to decrease. This shows that although miniaturization vastly decreases the performance capabilities of a PPT, there are few changes to the trends in performance predicted past PPT performance analyses.

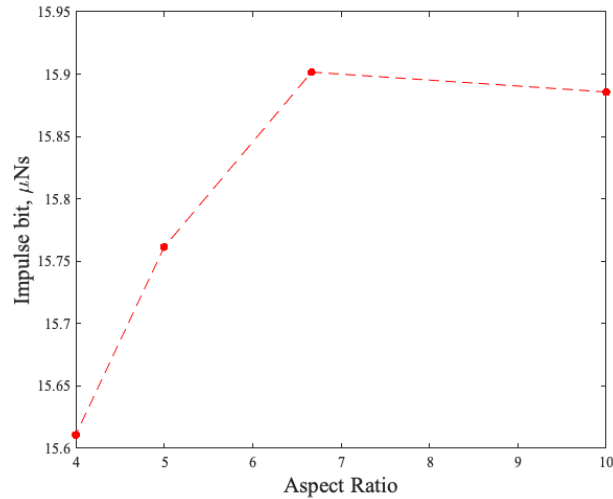


Figure 5.11 - Impulse bit as a function of an increasing aspect ratio by decreasing electrode width

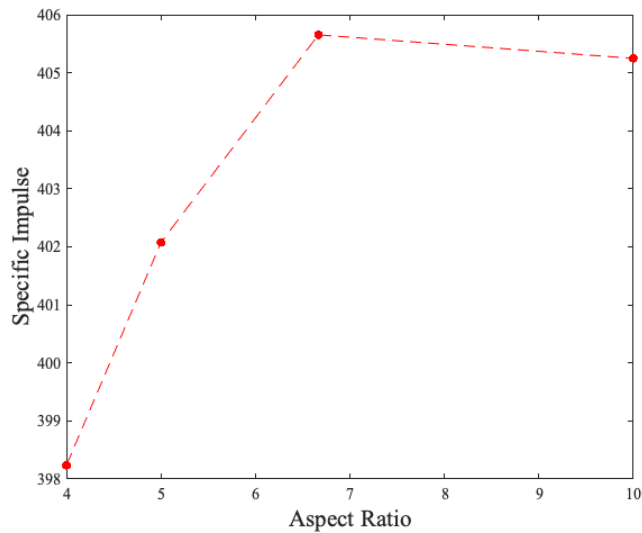


Figure 5.12 - Specific impulse as a function of an increasing aspect ratio by decreasing electrode width

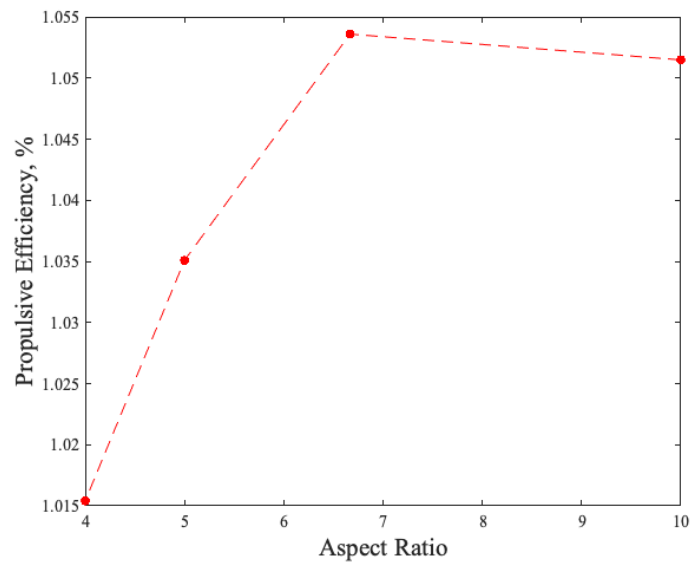


Figure 5.13 - Propulsive efficiency as a function of an increasing aspect ratio by decreasing electrode width

6 Conclusion

A μ PPT design was produced throughout this entire report which enabled a variety of electrode geometries to be investigated. The overall thruster's performance was evaluated for an electrode gap distance of 5 – 20 mm, an electrode width and thickness of 5 mm and electrode length of 20 mm, resulting in an aspect ratio range of 1 – 4, at a discharge energy of 3 J. This resulted in a performance that depended, heavily, on the aspect ratio and saw increases to the I_{bit} , I_{sp} , T_{sp} and η . This same trend was shown in a μ PPT of similar design. The discrepancy in performance between the two μ PPTs was likely due to the vastly different inductance values determined for each. Despite this, this μ PPTs overall performance exceeded that of the benchmarks.

Furthermore, this analysis showed the increases to these performance values relate to increasing AR by increasing h . Increasing the AR by decreasing the w actually results in the opposite being true for a μ PPT. These results agree with other μ PPT research and shows that miniaturization significantly decreases the magnitude of performance values but has little effect on the performance trends as geometry changes.

6.1 Future Considerations

Despite producing a successful design, the values for the performance were lower than the average PPT available. This is primarily due to the focus of this report being on identical straight parallel plate electrodes with a square cross-section. Based on the available data, this configuration results in the lowest performance among many other available configurations. Pottinger's own research includes an analysis of a rectangular and tongue electrode configuration with a flare angle of up to 60 degrees. This work results in an increase in I_{bit} of up to 500%. Any future research and experimentation done for μ PPTs should include an optimization of these configurations and investigate ways to increase the inductance gradient that are not already implemented in other designs.

References

- [1] Woellert, K., Ehrenfreund, P., Ricco, A. J., & Hertzfeld, H., “CubeSats: Cost-effective science and technology platforms for emerging and developing nations,” *Advances in Space Research*, 2nd ed., Vol. 47, No. 4, 2011, pp. 663–684. <https://doi.org/10.1016/j.asr.2010.10.009>
- [2] Nervold, A.K., Berk, J., Straub, J., Whalen, D., “A Pathway to Small Satellite Market Growth,” *Advances in Aerospace Science and Technology*, Vol. 1, No. 1, 2016, pp. 14-20. <http://dx.doi.org/10.4236/aast.2016.11002>
- [3] Nason, I., Puig-Suari, J., and Twiggs, R., "Development of a family of picosatellite deployers based on the CubeSat standard," *Proceedings, IEEE Aerospace Conference*, Big Sky, MT, USA, 2002, pp. 1-1. <https://doi.org/10.1109/AERO.2002.1036865>
- [4] Tummala, A. R., & Dutta, A., “An Overview of Cube-Satellite Propulsion Technologies and Trends,” *Aerospace*, Vol. 4, No. 4, 2017, pp. 58. <https://doi.org/10.3390/aerospace4040058>
- [5] Sobles, A., Thomassen, K., & Vondra, R. J., “Analysis of solid Teflon pulsed plasma thruster,” *Journal of Spacecraft and Rockets*, Vol. 7, No. 12, 1970, pp. 1402–1406. <https://doi.org/10.2514/3.30181>
- [6] Lemmer, K., “Propulsion for CubeSats,” *Acta Astronautica*, Vol. 134, 2017, pp. 231–243. <https://doi.org/10.1016/j.actaastro.2017.01.048>
- [7] Palumbo, D. J., & Guman, W. J., “Effects of Propellant and Electrode Geometry on Pulsed Ablative Plasma Thruster Performance,” *Journal of Spacecraft and Rockets*, Vol. 13, No. 3, 1976, pp. 163–167. <https://doi.org/10.2514/3.57077>
- [8] Pottinger, S. J., and Scharlemann, C. A., “Micro Pulsed Plasma Thruster Development,” 30th International Electric Propulsion Conference, Paper IEPC-2007-125, September 2007. <http://electricrocket.org/IEPC/IEPC-2007-125.pdf>
- [9] Kuang, Y. Z., “Experimental research of relationship between PPT parameters,” *International Electric Propulsion Conference*, 1985. <https://doi.org/10.2514/6.1985-2065>
- [10] Ou, Y., Wu, J., Zhang, Y., Li, J., & Tan, S., “Theoretical Modeling and Parameter Analysis of Micro-Pulsed Plasma Thruster,” *Energies*, Vol. 11, No. 5, 2018, pp. 1146. <https://doi.org/10.3390/en11051146>
- [11] Glascock, M. S., Rovey, J. L., & Polzin, K. A., “Electric Solid Propellant Ablation in an Arc Discharge,” *Journal of Propulsion and Power*, Vol. 35, No. 5, 2019, pp. 1-10. <https://doi.org/10.2514/1.B37517>
- [12] Burton, R. L., & Turchi, P. J., “Pulsed Plasma Thrusters,” *Journal of Propulsion and Power*, Vol. 14, No. 5, 2010, pp. 716-735. <https://doi.org/10.2514/2.5334>
- [13] Guarducci, F., Coletti, M., & Gabriel, S.B., “Design and Testing of a Micro Pulsed Plasma Thruster for CubeSat Application,” 32nd International Electric Propulsion Conference, Paper IEPC-2011-239, September 2011. <https://doi.org/10.1016/j.actaastro.2011.03.008>

- [14] Laystrom, J., Burton, R., & Benavides, G., “Geometric Optimization of a Coaxial Pulsed Plasma Thruster,” 39th Joint Propulsion Conference and Exhibit, AIAA Paper 2003-5025. June 2003. <https://doi.org/10.2514/6.2003-5025>
- [15] Kumagai, N., Sato, K., Tamura, K., Kawahara, K., Koide, T., & Takegahara, H., “Research and Development Status of Low Power Pulsed Plasma Thruster System for a μ -Lab Sat II,” 28th International Electric Propulsion Conference, Paper IEPC-03-2002, March 2003. <http://electricrocket.org/IEPC/0202-0303iepc-full.pdf>
- [16] Ling, W. Y. L., Zhang, S., Liu, X., Wang, N., Zhang, Z., & Tang, H., “A Study on Asymmetric Electrodes for Pulsed Plasma Thrusters,” 54th Joint Propulsion Conference, AIAA Paper 2018-4908, July 2018. <https://doi.org/10.2514/6.2018-4908>
- [17] Zhang, Z., Ren, J., Tang, H., Ling, W. Y. L., & York, T. M., “An ablative pulsed plasma thruster with a segmented anode,” *Plasma Sources Science and Technology*, Vol. 27, No. 1. <https://doi.org/10.1088/1361-6595/aa9e6b>
- [18] Dali, H., Wansheng, Z., & Xiaoming, K., “A study on the efficiency of pulsed plasma thruster (PPT),” *Aircraft Engineering and Aerospace Technology*, Vol. 78, No. 5, pp. 391–394. <https://doi.org/10.1108/00022660610685558>
- [19] Rahideh, H., Malekzadeh, P., & Golbahar Haghighi, M.R., “Non-Fourier Heat Conduction Analysis with Temperature-Dependent Thermal Conductivity,” *International Scholarly Research Notices*, Vol. 2011, 2011, pp. 1–10. <https://doi.org/10.5402/2011/321605>
- [20] Zhang, Y., Zhang, D., Wu, J., He, Z., & Zhang, H., “A novel laser ablation plasma thruster with electromagnetic acceleration,” *Acta Astronautica*, Vol. 127, 2016, pp. 438–447, <https://doi.org/10.1016/j.actaastro.2016.05.039>
- [21] Stechmann, D.P., Gatsonis, N., Juric, D., & Bryne, L., “Numerical Analysis of Transient Teflon Ablation in Pulsed Plasma Thrusters,” 43rd Joint Propulsion Conference and Exhibit, AIAA Paper 2007-5227, July 2007. <https://doi.org/10.2514/6.2007-5227>
- [22] Cho, M., & Sung, H.G., “Theoretical Modeling of Pulsed Plasma Thruster Performance with Teflon Ablation,” *International Journal of Aeronautical and Space Sciences*, Vol. 18, No. 1, 2017, pp. 138-143. <https://doi.org/10.5139/IJASS.2017.18.1.138>
- [23] Ciaralli, S., Coletti, M., & Gabriel, S. B., “Results of the qualification test campaign of a Pulsed Plasma Thruster for CubeSat Propulsion (PPTCUP),” *Acta Astronautica*, Vol. 121, 2016, pp. 314–322, <https://doi.org/10.1016/j.actaastro.2015.08.016>
- [24] Mingo Perez, A., Coletti, M., & Gabriel, S. B., “A micro PPT for Nano satellite applications: Design and experimental results,” 48th Joint Propulsion Conference and Exhibit, AIAA Paper 2012-4279. July 2012. <https://doi.org/10.2514/6.2012-4279>
- [25] Coletti, M., Gabriel, S. B., & Guarducci, F., “A micro PPT for CubeSat application: Design and preliminary experimental results” *Acta Astronautica*, Vol. 69, 2011, pp. 200-208, <https://doi.org/10.1016/j.actaastro.2011.03.008>
- [26] Woodruff, C. A., King, D. M., Burton, R. L., & Carroll, D. L., “Fiber-fed Pulsed Plasma Thruster (FPPT) for Small Satellites,” 36th International Electric Propulsion Conference, Paper IEPC-2019-A899, September 2019. <http://electricrocket.org/2019/899.pdf>

- [27] Busek Company Inc., “BmP-220 Technical Specifications”, Datasheet 70008502G
- [28] Ling, W. Y. L., Zhang, S., Fu, H., Huang, M., Quansah, J., Liu, X., & Wang, N., “A brief review of alternative propellants and requirements for pulsed plasma thrusters in micropropulsion applications”, *Chinese Journal of Aeronautics*, Vol. 33, No. 12, 2020, pp. 2999-3010. <https://doi.org/10.1016/j.cja.2020.03.024>
- [29] Rayburn, C., Campbell, M., Hoskins, W. A., & Cassady R. J., “Development of a Micro Pulsed Plasma Thruster for the Dawgstar Nanosatellite”, 36th Joint Propulsion Conference and Exhibit, AIAA Paper 2000-3256, July 2000. <https://doi.org/10.2514/6.2000-3256>
- [30] Molina-Cabrera P., Herdrich, G., Lau, M., Fausolas, S., Schoenherr, T., & Komurasaki, K., “Pulsed Plasma Thrusters: a worldwide review and long yearned classification”, 32nd International Electric Propulsion Conference, IEPC Paper 2011-340, September 2011. <http://electricrocket.org/IEPC/IEPC-2011-340.pdf>
- [31] Guman, W. J., & Nathanson, D. M., “Pulsed Plasma Microthruster Propulsion System for Synchronous Orbit Satellite”, *Journal of Spacecraft and Rockets*, Vol. 7, No. 4, 1970, pp. 409-415. <https://doi.org/10.2514/3.29955>
- [32] Gessini, P., Paccani, G., “Ablative Pulsed Plasma Thruster System Optimization for Microsatellites”, 27th International Electric Propulsion Conference, IEPC Paper 01-182, October 2001. http://electricrocket.org/IEPC/182_6.pdf
- [33] Tran, Q.-V., Lim, W.-S., Bui, T.-D.-V., Low, K.-S., & Kang, B., “Development of a Dual-axis Pulsed Plasma Thruster for Nanosatellite Applications”, *Journal of Small Satellites*, Vol. 8, No. 2, pp. 837-847. <https://jossonline.com/storage/2021/08/Final-Tran-Development-of-a-Dual-axis-Pulsed-Plasma-Thruster-for-Nanosatellite-Applications.pdf>
- [34] Bird, J., “Electrical and Electronic Principles and Technology”, *Capacitors and capacitance*, 5th ed., Vol. 1, Taylor & Francis, 2014, pp. 62-79.
- [35] Barquero, S., Martinez, M.M., “Pulsed Plasma Thruster Design”, *Interreg Sudoe: NANOSTAR*, 1st ed., Vol. 1, NANOSTAR Consortium https://nanostarproject.eu/wp-content/uploads/2020/10/UC3M_Pulsed-Plasma-Thruster-Design.pdf
- [36] Pottinger, S. J., Krejci, D., Scharlemann, C.A., “Pulsed plasma thruster performance for miniaturized electrode configurations and low energy operation”, *Acta Astronautica*, Vol. 68, No. 12, 2011, pp. 1996-2004. <https://doi.org/10.1016/j.actaastro.2010.11.011>
- [37] High Energy Devices LLC, “Use of Triggered Spark Gaps: Application Note”, Datasheet AN-TG-10, 2008 <https://www.highenergydevices.com/documents/AN-TG-10.pdf>
- [38] KEMET Electronics Corporation, “R75, Single Metallized Polypropylene Film, Radial, DC and Pulse Applications (Automotive Grade)”, Datasheet F3106-R75
- [39] Grover, F.W., “Parallel Elements of Equal Length”, *Inductance Calculations: Working Formulas and Tables*, 2nd ed., Vol. 1, Dover Publications, 2009, pp. 60-69
- [40] Lui, F., Nie, Z., Xu, X., Zhou, Q., Li, Q., & Liang, R., “Measurement of electron density by Stark broadening in an ablative pulsed plasma thruster”, *Applied Physics Letters*, Vol. 93, No. 11, 2008. <https://doi.org/10.1063/1.2983747>

Appendix A – MATLAB Code

Electrode Parameters

```
h = 0.005; hc = 0.5; % electrode gap, m;cm
w = 0.005; wc = 0.5; % electrode width, m;cm
d = 0.005; dc = 0.5; % electrode thickness, m;cm
l = 0.2; lc = 2; % electrode length, m;cm
t = linspace(0,10E-6,1000); % pulse span
t2 = 0;
AR = h/w;
```

Circuit Parameters

```
V0 = 1500; % discharge voltage, V
C = 2.7E-6; % capacitance, F
L_c = 0.007058E-6; % capacitor inductance, H
L_e = 7E-9; % lead and wire inductance, H
R_c = 0.000941; % capacitor resistance, ohms
R_e = 0.096; % lead and wire resistance, ohms
R_pe = 2*0.0000134; % plate electrode resistance, ohms
t_d = 4E-6; % discharge time (estimate), s

L_el = (0.002*lc*(log(2*lc/(wc+dc)) + 0.49823))*1E-6; % Electrode self-
inductance, H
L_p = (0.002.*hc*(log(2*hc/(wc+dc)) + 0.49823))*1E-6; % Plasma self-
inductance, H
M_el = (0.002*lc*(log(2*lc/hc) - 1 + (hc/lc) - (hc^2/(4*lc^2))))*1E-6;
% Electrode Mutual inductance, H
L_pe = 2*L_el + L_p - M_el; % Plate electrode inductance total
```

Plasma Parameters

```
T_e = 18000; % electron Temperature, K
n_e = 2.534e22; % electron number density, 1/m^3
```

```

mu0 = 12.57e-7; % vacuum permeability, H/m
sigma = 1.38064852E-23; % Boltzmann Constant, kgm^2 / Ks^2

```

Performance Study

```

m_bit = 4E-9;
g = 9.8;
E = 3;

R_p = (h/(w*T_e^(0.75)))*sqrt((mu0*log(1.24e7*(T_e^3/n_e)^(0.5)))/t_d);
% Plasma resistance
LT = L_c + L_e + L_pe; % total inductance, H
RT = R_c + R_e + R_pe + R_p; % total resistance, ohms
%LT = 145E-9;
L2 = (mu0/(2*pi))*(3/2 + log(h/(w+d))); % L'/2 part of the impulse bit
equation
%L21 = ((0.6 + 0.4*log(h/(w+d)))/2)*1E-6
Q = h*w*n_e*sigma*T_e*t_d; % gas dynamic component of the impulse bit

om = sqrt(1/(LT*C) - (RT^2)/(4*LT^2)); % omega term of current/voltage
functions
del = atan(sqrt(4*LT/(C*RT^2) - 1)); % delta term of the current/voltage
functions

cr = (C*RT^2)/(4*LT)
It = (V0/(om*LT)).*sin(om.*t).*exp(-RT*t./(2*LT));
Vt = ((V0)/(om*sqrt(LT*C))).*sin(om.*t + del).*exp(-RT*t./(2*LT));

fun = @(x) ((V0/(om*LT)).*sin(om.*x).*exp(-RT*x./(2*LT))).^2;
int = integral(fun,0,3E-6);

Ibit = L2*int + Q
Isp = Ibit/(g*m_bit)
e = g*Isp*Ibit/(2*E)

```

```
Tsp = Ibit/E
```

```
AR
```

Comparative Plots

```
t1 = linspace(0,10E-6,1000)
tau = 5E-6;
Cppt = 6E-6;
I1 = 3.2E3;
I2 = 800;
V01 = 816.5;

L1 = (tau^2)/(4*pi^2*Cppt)
R1 = (4*L1/tau)*log(I1/I2)
del1 = atan(sqrt(4*L1/(Cppt*R1^2) - 1))
om1 = sqrt(1/(L1*Cppt) - (R1^2)/(4*L1^2))

It1 = (V01/(om1*L1)).*sin(om1.*t1).*exp(-R1*t1./(2*L1));
Vt1 = ((V01)/(om1*sqrt(L1*Cppt))).*sin(om1.*t1 + del1).*exp(-R1*t1./(2*L1))

% Change plot axis to micro-seconds
t4 = t*1E6;
t5 = t1*1E6;

figure,
hold on
plot(t4,It,'r','LineWidth',2)
plot(t5,It1,'b','LineWidth',2)
set(gca,'FontSize',14,'FontName','Times New Roman')
lgd = legend('Design','Pottinger',Location='best');
lgd.FontSize = 16;
lgd.FontName = 'Times New Roman';
ylabel('Current, A','FontName','Times New Roman','FontSize',21)
```

```

xlabel('Time, \mus', 'FontName', 'Times New Roman', 'FontSize', 21)
hold off

figure,
hold on
plot(t4, Vt, 'r', 'LineWidth', 2)
plot(t5, Vt1, 'b', 'LineWidth', 2)
set(gca, 'FontSize', 14, 'FontName', 'Times New Roman')
lgd = legend('Design', 'Pottinger', Location='best');
lgd.FontSize = 16;
lgd.FontName = 'Times New Roman';
ylabel('Voltage, V', 'FontName', 'Times New Roman', 'FontSize', 21)
xlabel('Time, \mus', 'FontName', 'Times New Roman', 'FontSize', 21)
hold off

```

Pottinger Data

```

Ibp = [6.5 7.4 8.38 9.31 10.25];
Cpp = 6E-6;
Lpp = [145E-9 152.2E-9 159.4E-9 166.6E-9 173.8E-9];
Rpp = [55.1E-3 66.425E-3 77.75E-3 89.075E-3 100.4E-3];

m_bp = 3E-9; % kg
Ep = 2;
Ispp = (Ibp./1E6)./(g*m_bp);
ep = g.*Ispp.*(Ibp./1E6)./(2*Ep);

crp = (Cpp.*Rpp.^2)./(4.*Lpp)

```

Plots

```

figure,
hold on
box on

```

```

plot(AR,cr,'--r.','MarkerSize',20)
plot(AR,crp,'--b.','MarkerSize',20)
set(gca,'FontSize',14,'FontName','Times New Roman')
lgd = legend('Design','Pottinger',Location='best');
lgd.FontSize = 16;
lgd.FontName = 'Times New Roman';
xlabel('Aspect Ratio','FontName','Times New Roman','FontSize',21)
ylabel('Damping Ratio','FontName','Times New Roman','FontSize',21)
hold off

figure,
hold on
box on
plot(AR,Ibit,'--r.','MarkerSize',20)
plot(AR,Ibp,'--b.','MarkerSize',20)
set(gca,'FontSize',14,'FontName','Times New Roman')
lgd = legend('Design','Pottinger',Location='best');
lgd.FontSize = 16;
lgd.FontName = 'Times New Roman';
xlabel('Aspect Ratio','FontName','Times New Roman','FontSize',21)
ylabel('Impulse bit, \muNs','FontName','Times New Roman','FontSize',21)
hold off

figure,
hold on
box on
plot(AR,Isp,'--r.','MarkerSize',20)
plot(AR,Isp,'--b.','MarkerSize',20)
set(gca,'FontSize',14,'FontName','Times New Roman')
lgd = legend('Design','Pottinger',Location='best');
lgd.FontSize = 16;

```

```

lgd.FontName = 'Times New Roman';
xlabel('Aspect Ratio','FontName','Times New Roman','FontSize',21)
ylabel('Specific Impulse','FontName','Times New Roman','FontSize',21)
hold off

figure,
hold on
box on
plot(AR,e,'--r.','MarkerSize',20)
plot(AR,ep,'--b.','MarkerSize',20)
set(gca,'FontSize',14,'FontName','Times New Roman')
lgd = legend('Design','Pottinger',Location='best');
lgd.FontSize = 16;
lgd.FontName = 'Times New Roman';
xlabel('Aspect Ratio','FontName','Times New Roman','FontSize',21)
ylabel('Propulsive Efficiency','FontName','Times New Roman','FontSize',21)
hold off

```